The gut microbiome-linked long chain fatty acid stearate suppresses colorectal cancer

Mina Tsenkova[1], Madita Brauer[1,2], Vitaly Pozdeev[1], Marat Kasakin[3], Susheel Bhanu Busi[3,4], Maryse Schmoetten[1], Dean Cheung[1], Marianne Meyers[1], Fabien Rodriguez[1], Anthoula Gaigneaux[5], Eric Koncina[1], Cedric Gilson[1], Lisa Schlicker[3], Diran Herebian[6], Martine Schmitz[1], Laura de Nies[3], Ertan Mayatepek[6], Serge Haan[1], Carine de Beaufort[7], Thorsten Cramer[8], Johannes Meiser[9], Carole L. Linster[3], Paul Wilmes[3,5], Elisabeth Letellier[1]

[1] Molecular Disease Mechanisms Group, Department of Life Sciences and Medicine, Faculty of Science, Technology and Medicine, University of Luxembourg, Esch-sur-Alzette, Luxembourg

[2] Institute for Advanced Studies, University of Luxembourg, Esch-sur-Alzette, Luxembourg

[3] Luxembourg Centre for Systems Biomedicine, University of Luxembourg, Esch-sur-Alzette, Luxembourg

[4] UK Centre for Ecology and Hydrology, Wallingford, United Kingdom

[5] Department of Life Sciences and Medicine, Faculty of Science, Technology and Medicine, University of Luxembourg, Esch-sur-Alzette, Luxembourg

[6] Department of General Pediatrics, Neonatology and Pediatric Cardiology, Medical Faculty and University Hospital Düsseldorf, Heinrich Heine University, Düsseldorf, Germany

[7] Pediatric Clinic, Centre Hospitalier de Luxembourg, Luxembourg, Luxembourg

[8] Molecular Tumor Biology, Department of General, Visceral and Transplantation Surgery, RWTH University Hospital Aachen, Germany

[9] Department of Cancer Research (DOCR), Luxembourg Institute of Health, Luxembourg, Luxembourg

Abstract

Colorectal cancer (CRC) patients have been shown to possess an altered gut microbiome. Diet is a well-established modulator of the microbiome, and thus, dietary interventions might have a beneficial effect on CRC. An attenuating effect of the ketogenic diet (KD) on CRC cell growth has been previously observed, however the role of the gut microbiome in driving this effect remains unknown. Here, we describe a reduced colonic tumor burden upon KD consumption in a CRC mouse model with a humanized microbiome. Importantly, we demonstrate a causal relationship through microbiome transplantation into germ-free mice, whereby alterations in the gut microbiota were maintained in the absence of continued selective pressure from the KD. Specifically, we identify a shift toward bacterial species that produce stearic acid in ketogenic conditions, whereas consumers were depleted, resulting in elevated levels of free stearate in the gut lumen. This microbial product demonstrated tumor-suppressing properties by inducing apoptosis in cancer cells and decreasing colonic Th17 immune cell populations. Taken together, the beneficial effects of the KD are mediated through alterations in the gut microbiome, including, among others, increased stearic acid production, which in turn significantly reduces intestinal tumor growth.

44 **Introduction**

45 Worldwide, colorectal cancer (CRC) is the third most prevalent cancer, with over 1.9 million new
46 cases recorded in 2020[1]. CRC incidence and mortality rates have been associated with various lifestyle-
47 related risk factors, in particular dietary habits. Recent years have seen a rise in CRC incidence in persons
48 aged 50 years and under, further underlining the importance of studying these factors[2]. The ketogenic
49 diet (KD) has been shown to possess anti-cancer properties in the context of CRC, and many studies have
50 focused on the importance of the restriction of energy intake to slow the growth of rapidly proliferating
51 cells and anti-cancer signaling through ketone bodies[3]. One recently published study investigated the
52 effects of the KD on CRC development and described a new mechanism through which KD exerts its anti-
53 cancer effects, namely through the ketone body β-hydroxybutyrate acting on the surface receptor Hcar2,
54 inducing the transcriptional regulator *Hopx*, thus altering gene expression and inhibiting cell proliferation[4].
55 These studies often focus on the effects of KD on the cancer cells themselves, and rarely on other cells of
56 the tumor microenvironment (TME), such as immune cells[5,6] and cancer-associated fibroblasts (CAFs)[7], or
57 on external factors, such as the gut microbiome. Specifically in CRC, cancer progression is accompanied
58 by a state of dysbiosis of the gut microbiome[8–10]. The study of the role of the different bacteria in CRC is
59 of particular interest, considering the affected tissue type is in contact with the gut microbiome. Until
60 recently, few studies had investigated the effects of the KD on the gut microbiome in health and disease[11],
61 but this has now changed, with a number of new studies published over the last three years[6,8]. These
62 studies remain largely descriptive regarding dietary-induced gut microbiome changes and the role of the
63 gut microbiome in maintaining the reported anti-cancer effects of the KD in the context of CRC has not
64 yet been investigated. Therefore, we set out to investigate the importance of the gut microbiome in the
65 context of KD consumption in CRC. We first generated a humanized gut microbiome mouse model of CRC,
66 through the transplantation of stool samples from five healthy human donors. We then combined this
67 model with a therapeutically administered KD and were able to confirm the cancer-suppressing properties

68 of the KD. Most importantly, we could demonstrate, for the very first time, the causal role of the gut
69 microbiome in maintaining this effect, through transplantation of the microbial community. We report
70 long-lasting alterations in gut microbiome function in the absence of maintained selective pressure by the
71 KD. In our experiments, fecal free stearic acid levels were increased not only upon KD consumption, but
72 also upon cecal transplantation, suggesting that the shift in the microbial community contributes to the
73 changes in the fatty acid pool. Importantly, stearate-producing members were enriched in ketogenic
74 conditions, whereas consumers were depleted and supplementation of stearic acid reduced tumor
75 burden *in vivo*.
76

77 **Results**

78 **KD leads to reduced colonic tumor burden and inflammatory response in CRC**

79 To study the relevance of the gut microbiome in CRC development in a model relevant to human
80 disease, we first established a representative healthy human microbiome by mixing fecal samples from
81 five healthy donors (5HD; Extended Data Fig. 1a for patient metadata). The achieved 5HD mix
82 recapitulated the compositions of the individual donor samples, as evidenced by family, genus and species
83 level analysis of whole genome shotgun sequencing (WGS, Extended Data Fig. 1b-d, respectively), while
84 fecal metabolite levels varied across samples (Extended Data Fig. 1e). We performed fecal microbial
85 transplantation (FMT) of the 5HD mix into germ-free (GF) and antibiotic-treated specific-pathogen-free
86 (SPF) mice in an AOM/DSS CRC model (Fig. 1a and 1b, details can be found in the methods section)
87 followed by a switch from standard to ketogenic diet after the last cycle of DSS. We utilized both GF and
88 SPF mice to leverage the fully functional immune system of SPF mice to study immune responses in CRC
89 and the unique advantage of GF mice allowing engraftment of a human microbiome into mice in the
90 absence of competition with a resident mouse microbiome. Antibiotic-treated SPF mice were subjected
91 to bi-weekly FMT during the induction of CRC to maintain enrichment of the donor fecal microbiome in

92 relation to the residual host mouse microbiome. FMT was ceased at diet change to allow for a natural
93 evolution of the gut microbiome in response to the diet and CRC progression. No significant difference in
94 body weight between the standard diet (SD) and ketogenic diet (KD) groups was observed throughout the
95 experiments, although dips in mouse body weight were observed following the antibiotic treatment and
96 following each cycle of DSS (Extended Data Fig. 2a (GF) and 2b (SPF)). There was no difference in colon
97 length between groups (Extended Data Fig. 2c, GF). KD-fed mice exhibited a lower colonic tumor burden
98 (Fig. 1c (GF) and Fig. 1d (SPF)) and a smaller tumor size (Fig. 1e, 1f and 1g (SPF)) than SD-fed mice.

99 Characterization of full-length lamina propria (LP), mesenteric lymph node (MLN) and spleen
100 immune cell profiles (Extended Data Fig. 2d (GF) and 2e (SPF)) showed a reduction in LP $CD4^+$ T cell
101 populations in KD-fed mice. We particularly observed a decrease in Th17 cells (Extended Data Fig. 2f), a
102 pathogenic subpopulation of $CD4^+$ T cells known to play a critical role in CRC development as evidenced
103 by reduced expression of IL-6, STAT3, IFNγ, and TNFα, leading to fewer and smaller tumors in IL-17A-
104 deficient mice[12]. Only LP natural killer T cells and type 3 innate lymphoid cells (GF LP) were increased –
105 both have been associated to gut homeostasis and health[13]. The expression of colonic S100A8, a subunit
106 of calprotectin (a biomarker of inflammation used in inflammatory bowel disease[14]), as well as fecal
107 lipocalin-2 were however unchanged in KD-fed mice, suggesting an overall similar inflammatory milieu
108 (Extended Data Fig. 2g (GF), h and i (SPF)). Thus, it remains unclear whether the observed reduction in
109 immune cell populations is a result mediated by the KD or if it is a direct consequence of decreased tumor
110 development. Conducting time-course analyses at various stages of the AOM/DSS-induced carcinogenic
111 process would be essential to elucidate the temporal sequence of events leading to the observed
112 reduction in colonic tumor burden.

113 To further assess the importance of KD in modulating inflammation in CRC, we employed a low-grade
114 inflammatory model, in which mice received four doses of AOM and were randomized into two subgroups
115 - GF and 5HD mix FMT, each with a KD and SD branch (Extended Data Fig. 3a-b). We did not observe any

116 significant differences in colonic tumor burden between groups (Extended Data Fig. 3c), nor in immune
117 cell profiles (Extended Data Fig. 3d), suggesting that the KD specifically exerted its anti-cancer effect in an
118 inflammatory setting. The differences in immune populations between the KD and SD in the AOM/DSS
119 model, which are absent in this low-grade inflammatory model, may be due to the lack of damage-
120 associated molecular patterns (DAMPs) from DSS-induced epithelial damage. This suggests that the KD
121 attenuates chronic inflammation activated by such damage, potentially leading to a reduced tumor
122 burden in this inflammation-driven CRC model. Of note, long-term KD feeding induced fatty liver and
123 fibrosis in all sub-groups (Extended Data Fig. 3e), and as previously reported for long-term KD
124 consumption[15].

125

126 **KD induces a distinct host metabolic profile**

127 Ordination analyses based on the underlying β-diversity among host plasma samples collected
128 from animals undergoing ketogenic dietary intervention in the AOM/DSS inflammatory model of CRC,
129 revealed clustering based on dietary condition (Extended Data Fig. 4a (GF) and Extended Data Fig. 4b
130 (SPF)). β-HB plasma levels were elevated in KD-fed mice (Extended Data Fig. 4c (GF) and 4d (SPF)),
131 confirming ketosis. KD-fed mice presented altered amino acid, fatty acid, sugar, carbohydrate, vitamin,
132 and bile acid metabolism (Supp. Table 1 and Extended Data Fig. 4e (GF), Supp. Table 2 and Supp Fig. 4f
133 (SPF). Furthermore, mannose was increased in KD-fed mice (Supp. Tables 1 (GF) and 2(SPF)). Interestingly,
134 mannose has been reported to possess antitumor properties[16], impairing tumor cell growth *in vitro* and
135 *in vivo*[17], and targeting tumor-associated macrophages[18]. While treatment with β-hydroxybutyrate
136 showed no effect, treatment with the ketone bodies acetone and sodium acetoacetate tended to reduce
137 the differentiation of naive T cells into Th17 cells (Extended Data Fig. 4g and 4h), which play an important
138 role in the modulation of colorectal tumorigenesis[19] and are affected by KD in a dose-dependent manner[5].
139 Treatment with a commercially available lipid mixture mimicking KD (containing arachidonic, linoleic,

140 linolenic, myristic, oleic, palmitic and stearic acid) led to a dose-dependent reduction in Th17
141 differentiation (Extended Data Fig. 4i), suggesting that Th17 cells are susceptible to fatty acid modulation.
142 Collectively, these data indicate that KD induces systemic functional metabolic changes in the host, which
143 are not limited to the induction of ketosis.
144
145 **The anti-cancer effects of the KD are mediated by the gut microbiome**
146 The gut microbiome may affect CRC development either by directly interacting with host cells
147 (attachment, invasion and translocation), or indirectly, through bacterial metabolism (genotoxins, SCFAs
148 and others)[20]. We first excluded bacterial translocation as a primary factor in the KD-mediated phenotype,
149 as mucus layer thickness (Extended Data Fig. 5a and 5b (GF)), LPS levels in plasma (Extended Data Fig. 5c
150 (GF) and 5d (SPF)), and occludin expression (Extended Data Fig. 5e and 5f (SPF)) remained unaltered upon
151 KD consumption, in line with Ang et al.[5] We next performed cecal microbial transplantation (CMT) of
152 samples collected from the SPF diet mice (Fig. 1d) into a next generation of SD-fed GF mice undergoing
153 the same cancer model (Fig. 2a, Extended Data Fig. 6a). We did not observe a statistically significant
154 difference in colonic occludin expression in ketogenic cecal recipient mice (KC, Extended Data Fig. 6b and
155 6c) when compared to standard cecal recipients (SC), however we did detect a decrease in S1008A levels
156 (Extended Data Fig. 6d). Strikingly, KC mice exhibited a lower colonic tumor burden than SC mice (Fig. 2b).
157 Average colonic tumor size per mouse did not differ between groups (Fig. 2c), however, KC mice exhibited
158 a smaller proportion of large tumors (Fig. 2d and e). Altogether, our results demonstrate the causal role
159 of the gut microbiome in mediating the previously observed KD-driven anticancer effect.
160
161 **KD induces a distinct fecal microbial profile**
162 Ordination analyses based on the underlying β-diversity among fecal samples collected from KD-
163 and SD-fed AOM/DSS mice revealed clustering of 5HD mix used for FMT with the individual healthy donor

164 stool samples and with the murine stool samples collected three days after FMT (TG, Fig. 3a (GF) and 3b
165 (SPF)), confirming the validity of the 5HD mix used for transplant and its engraftment. Furthermore, we
166 observed increasing differences between KD and SD samples over time (Fig. 3c (GF) and 3d (SPF)). Early
167 time points cluster together (T0, collected at diet change), while later time points diverge (T1-T4).
168 Differential analysis revealed *Phocea* spp., *Faecalitalea* spp. (Fig. 3e (GF), Supp. Tables 3 (GF) and 4 (SPF))
169 and *Akkermansia* spp., *Intestimonas* spp., *Lachnoclostridium* spp., *Bilophila* spp. and others (Fig. 3f (SPF)),
170 to be more abundant in KD, while *Barnesiella* spp., *Eisenbergiella* spp., *Ruminococcus 1* and *2* spp. (GF),
171 and *Bifidobacterium* spp., *Turicibacter* spp. (SPF), and others were depleted. Furthermore, the differential
172 abundance of various members of *Barnesiellaceae* spp., *Erysipelotrichaceae* spp., *Lachnospiraceae* spp.
173 and *Ruminococcaceae* spp. suggested that dietary composition affects bacterial members of the same
174 families in different manners.

175 Investigation of the engrafted gut microbial communities at experimental endpoint revealed
176 distinct KD- and SD-associated microbiomes (Fig. 3g and 3h), as well as KC- and SC-associated microbiomes
177 (Fig. 3g and 3h). Although a selective pressure of the KD was observed, gut microbial composition differed
178 between cecal donor and recipient mice, likely due to the absence of continued selective pressure from
179 the KD, or loss of more sensitive and hard-to-engraft bacteria (Fig. 3g). Metagenome-assembled genomes
180 (MAGs), representing abundant members of the microbial community, allowed us to achieve species-level
181 resolution. Noteworthy, some MAGs annotated as CRC-associated bacteria, such as *Rikenellaceae* spp.
182 (light blue) and *Muribaculaceae* spp. (dark blue, Fig. 3i), were detected in standard but not in ketogenic
183 conditions. Interestingly, various *Alistipes* spp. were differentially abundant in all experiments. However,
184 the genus Alistipes was only recently described, and although the genus has since then been linked to
185 various diseases, including colitis and CRC, the role of Alistipes in disease is still unclear[21]. Two MAGs
186 (*Alistipes* and *COE* species) were only identified in KC, while 12 MAGs were only identified in SC, among

187 which *CAG-873*, *CAG-48* and *Parabacteroides distasonis* (Fig. 3i), also identified in the donor SPF dietary
188 experiment.
189
190 **Distinct fecal microbial functional profiles are maintained upon FMT**
191 As microbiome-mediated effects are based on the functional and metabolic capacities of different
192 microbes, we investigated the fecal metabolic profiles of KD- versus SD-fed and KC- versus SC mice,
193 considering these profiles as a direct indicator of changes in the functional capacity of the different
194 microbial communities. Analysis of fecal metabolites revealed distinct clustering of samples by condition
195 in both the SPF dietary and CMT experiments (Fig. 4a and 4b, respectively). Mice in the ketogenic
196 conditions presented altered amino acid, fatty acid, carbohydrate and SCFA profiles (Supp. Tables 5 and
197 6), albeit to a lesser extent in the CMT experiment. A single detected long-chain fatty acid (LCFA), namely
198 free stearic acid (C18:0, also known as octadecanoic acid or stearate), was elevated in KD (Fig. 4c,
199 Extended Data Fig. 7a) and KC (Fig. 4d) mice. Strikingly, free stearic acid levels correlated with colonic
200 tumor burden in the SPF dietary experiment (Fig. 4e), with a similar trend observed in the CMT experiment
201 (Fig. 4e), suggesting a functional relevance of LCFA metabolism in CRC.
202
203 **KD induces a shift toward stearic acid production, which is maintained upon FMT**
204 To assess whether and how the microbiome contributes to shaping the LCFA pool, specifically
205 stearic acid, we focused on microbial LCFA metabolism. Most bacteria can produce LCFAs, which are
206 essential bacterial membrane components and signaling molecules. LCAFs are produced in a multistep
207 process by enzymes that are highly conserved among bacteria (Fig. 5a). Nevertheless, membrane LCFA
208 profiles differ between microbial taxa, varying for instance in chain length and degree of saturation[22]. To
209 investigate how the shift in the microbial communities reported in Fig. 3 affected the intestinal LCFA pool
210 in KD-fed and KC mice, we first mapped our metagenomic sequences against the Kyoto Encyclopedia of

211 Genes and Genomes (KEGG) database to obtain a list of contigs carrying LCFA metabolism-associated
212 KEGG orthologs. These contigs were further annotated at the taxonomic level using Kraken2 to estimate
213 the contribution of different microbial classes to LCFA metabolism in the different dietary conditions.
214 Consistent with the taxonomic shift reported in Fig. 3i, the relative contribution of bacteria from the class
215 Clostridia was higher in the KD groups, while members of the Bacteroides were diminished resulting in
216 less LCFA metabolism-associated contigs assigned to this class (Extended Data Fig. 7b). Specifically, contigs
217 carrying the microbial acyl-CoA thioesterases TesA and FatA (Fig. 5b) — enzymes required for the release
218 of free LCFAs, such as stearic acid, from the acyl-carrier[23] — were more frequently assigned to species
219 from the class Clostridia in the KD groups compared to the SD groups. This suggests that in the KD groups,
220 members of the class Clostridia may have contributed more significantly to the intestinal free LCFA pool
221 (Extended Data Fig. 7b). To investigate whether stearic acid is produced by Clostridia, we analyzed a
222 dataset published by Han et al.[24], who recently profiled the metabolome of bacterial culture supernatants.
223 Visualization of log2 fold changes in stearic acid levels in these supernatants revealed that *Bacteroidaceae*
224 and *Tannerellaceae* — two families within the class Bacteroidia — predominantly consume stearic acid *in*
225 *vitro*. In contrast, families form the class Clostridia, such as *Lachnospiraceae* and *Ruminococcaceae*,
226 release stearic acid into the culture supernatants (Fig. 5c). Notably, these families, although not
227 necessarily predominant in the communities, were consistently enriched or depleted across experiments
228 in KD and KC mice, respectively (Fig. 5d). Furthermore, the analysis of two other abundant LCFAs, palmitic
229 and oleic acid, showed that palmitic acid was consumed by most bacteria, with the exception of some
230 *Clostridaceae*, while oleic acid was released by all bacteria. This finding suggest that stearic acid is a family-
231 specific LCFA among the three analyzed LCFAs (Extended Data Fig. 7c). To further confirm that the source
232 of elevated free stearic acid in the mouse fecal samples was not coming from pre-existing differences in
233 stearic acid levels in the diets themselves, we profiled LCFA content in the SD and KD and confirmed similar
234 levels of free stearic acid (Extended Data Fig. 7d).

235 **Stearic acid reduces colonic tumor burden by inducing apoptosis in cancer cells**

236 To further investigate the role of stearic acid in CRC development, we supplemented stearic acid
237 through the dietary regimen to mice undergoing the same AOM/DSS CRC model described above (Fig. 6a,
238 6b and Extended Data Fig. 8a) and confirmed increased free stearic acid levels in the stearate-
239 supplemented diet compared to the control diet (Extended Data Fig. 8b). Mice on stearate-supplemented
240 diet (SSD) also exhibited elevated stearic acid serum and fecal levels (Fig. 6c and d, Supp. Tables 7 and 8).
241 We observed a reduction in colonic tumor burden (Fig. 6e and 6f), indicating that stearic acid exerts an
242 anti-tumorigenic effect in the development of CRC. We did not observe any difference in fecal lipocalin-2
243 levels between groups (Extended Data Fig. 8c), however, we further linked the reduced tumor burden to
244 decreased Th17 cells in vivo (Extended Data Fig. 8d). Furthermore, subsequent T cell differentiation assays
245 demonstrated that stearic acid supplementation specifically inhibited differentiation of $CD4^+$ T cells into
246 Th17 cells, a response not observed with other lipids (Extended Data Fig. 8e and 8f).

247 Treatment of various CRC cell lines with increasing concentrations of stearic acid led to a dose-
248 dependent reduction in cell growth (Fig. 6g and 6h, Extended Data Fig. 8g, 8h, 8i, 8j), highlighting stearic
249 acid as an anti-cancer metabolite which exerts direct effects on tumor cells. Furthermore, this observation
250 was specific to stearic acid, as treatment with other LCFAs did not exhibit anti-cancer properties (Fig. 6i).
251 We then performed RNA sequencing on HT-29 CRC cells treated with stearic, oleic and dodecanoic acids
252 to investigate the molecular mechanisms underlying the observed anti-cancer effect. Gene set
253 enrichment analysis (GSEA) suggested an arrest of cell proliferation and the induction of apoptosis upon
254 stearic acid treatment (Fig. 6k and 6l). Furthermore, stearic acid treatment was able to revert cell cycle
255 and apoptosis related gene expressions observed in control (vector-treated) cancer cells, which are in line
256 with those observed in patient tumor samples compared to matching normal tissue samples in the TCGA
257 dataset (Fig. 6l, Extended Data Fig. 8k). The use of a broad caspase inhibitor was able to abrogate the

258 effects of stearic acid treatment, confirming the underlying mechanism of stearic acid-induced cancer cell
259 death (Fig. 6m and n).
260
261 **Discussion**

262 The importance of the composition and function of the intestinal microbiome can be observed in
263 different disease contexts. Interestingly, recent studies have emphasized that the therapeutic response
264 in cancer is linked to specific bacterial functions, rather than individual bacterial species, suggesting that
265 microbial-derived metabolites play a critical role in driving the effectiveness of therapy[25–27]. In this study
266 we first identified the gut microbiome as a driving factor in the anti-cancer effect of KD in CRC. We next
267 demonstrated that KD alters gut microbial composition and metabolism. Upon KD consumption and
268 following microbial transplantation, we observed an increase in fecal free stearic acid, a LCFA, which
269 showed direct cancer-suppressing effects through the induction of apoptosis in cancer cells, as well as
270 indirect cancer-suppressing effects through suppression of pathogenic colonic Th17 cells.

271 The gut microbiome plays a key role in mediating the anti-cancer effects of the KD in the context
272 of a murine model of inflammation-driven CRC. However, the variability in the response observed (Figure
273 2b) suggests that the initial microbiome profile may determine whether an individual is a "responder" or
274 "non-responder" to KD. This concept, explored in epilepsy patients undergoing KD therapy for the
275 reduction of seizures[28] and in cancer treatments like immune checkpoint inhibition, highlights the
276 importance of the gut microbiome. Future studies should focus on identifying biomarkers to predict
277 response and strategies to convert "non-responders" into "responders," paving the way for personalized
278 treatments.

279 The depletion of dietary carbohydrates is known to provide a growth advantage for certain
280 bacteria, such as *Alistipes* spp., *Bilophila* spp. and mucin-degraders like *Akkermanisa* spp., whereas
281 *Bifidobacterium* spp. and some *Bacteroides* spp. are typically depleted[5,29], most likely due to their

282 preference for dietary carbohydrates over host glycans[30–32]. However, differences observed in
283 experiments investigating carbohydrate restriction and KD as intervention strategy suggest that limiting
284 carbohydrates is not the sole factor responsible for the beneficial effects of the KD. In our study, the
285 analysis of the fecal metabolomes in the KD dietary intervention and CMT experiments identified
286 differences in the LCFA pool, which are directly linked to different microbiome composition and metabolic
287 activity. In addition to their essential role in membrane biogenesis, LCFAs produced by bacteria have
288 signaling functions and play an essential role in host-microbe interactions[33]. The LCFA profile is highly
289 species-, or even strain-, and substrate-dependent and various microbial-derived LCFAs have different
290 effects linking bacterial LCFA metabolism to host health and disease[22,33]. Amongst others, microbiome-
291 derived LCFAs have an immunomodulatory potential[33,34]. We specifically identified stearic acid, a LCFA, in
292 KD and KC mice, which can originate from the diet, the host[35] and the gut microbiome[36]. We observed the
293 stearic acid to be specifically increased in the fecal samples of the KD-fed mice and not in the circulatory
294 system, suggesting that it is not a systemic effect of the KD but rather that it is the KD-driven changes in
295 the gut microbiome that led to differences in stearic acid.

296 Stearic acid is normally desaturated by the host enzyme SDC1[37], which is downregulated upon
297 reduced glucose intake and has been linked to inflammation[38–40]. Recently, Kindt et al. showed that
298 microbiome-derived acetate activated SDC1 and promoted LCFA desaturation[41]. Furthermore, certain
299 members of the gut microbiome can directly affect stearic acid levels by producing it *de novo* or
300 transforming it from other LCFAs, such as oleic acid[36], or by acquiring it as an exogenous LCFA for
301 downstream use in membrane lipid synthesis, or LCFA degradation[42,43]. In our experiments, as free fecal
302 stearic acid levels were increased not only upon KD consumption, but also in KC, it is likely that the shift
303 in the microbial community is contributing to the changes in the LCFA pool. Importantly, potential
304 stearate-producing members were enriched by the KD, whereas consumers were depleted (Fig. 5b-d),
305 leading to increased free stearic acid levels in the gut lumen.

306 Finally, we investigated the effects of stearic acid in our humanized CRC mouse model. Through a
307 stearic acid-enriched dietary intervention, we demonstrated that stearic acid effectively inhibits tumor
308 growth both directly, by inducing apoptosis in cancer cells, and indirectly, by reducing the recruitment of
309 pro-tumorigenic Th17 cells. In previous studies, stearic acid inhibited colony formation in different human
310 cancer cell lines[44], reduced tumor burden in a rat model of mammary carcinoma[45], possibly by inducing
311 apoptosis via signaling through protein kinase C[46], and suppressed CRC in synergy with 5-FU treatment[47].
312 Taken together, our study highlights the significant role of the gut microbiome and its derived
313 metabolites, in particular stearic acid, in mediating the KD's anti-tumorigenic effects. Most importantly,
314 our findings suggest that oral supplementation with a single metabolite could enhance existing treatment
315 strategies for CRC.
316
317 **Methods**

318 *Human sample collection*

319 Human samples were obtained and handled in accordance with institutional guidelines. All human
320 samples used in this project were donated freely, upon informed consent. Ethical approval was given by
321 the Comité National d'Ethique de Recherche of Luxembourg (MuSt authorization number 201110/05) and
322 the National Commission for Data Protection in Luxembourg. Samples were collected at the donors'
323 homes in accordance with the standard practices established by the Integrated Biobank of Luxembourg
324 (IBBL), in feces collection tubes, then aliquoted and stored at -80°C until further use.
325

326 *In vivo mouse experiments*

327 Animal experiments were performed according to all applicable laws and regulations, with
328 approval from the Animal Experimentation Ethics Committee (AEEC) and the veterinary service of the
329 Ministry of Agriculture, Viticulture and Rural Development of Luxembourg (LUPA2019-13). They ensure

330 that the care and the use of the animals for research purposes is conducted according to the European
331 Union (EU) Directive 2010/63/EU and to the Grand-Ducal Regulation of the 11th of January 2013,
332 regarding the protection of animals used for experimentation. This includes justification for the use of the
333 animals, guidelines for their care and welfare, and the incorporation of the 3Rs (replacement, reduction
334 and refinement). All mouse experiments were carried out at the animal facility of the Luxembourg Centre
335 for Systems Biology (LCSB).

336 C57BL/6J mice were purchased from Charles River France. C57BL/6NTac mice were bred in house.
337 C57BL/6J mice were housed in AllenTown NexGen Mouse 500 (19.4 cm x 13.0 cm x 38.1 cm) cages with
338 JRS Rehofix Corncob bedding, while C57BL/6NTac mice were housed in AllenTown Sentry Sealed Positive
339 Pressure Individually Ventilated (SPP IVC) cages (13.3 cm x 12.8 cm x 32.5 cm). Food and water were
340 provided *ad libitum*. Animals were maintained on standard rodent chow (A04, SAFE Lab, irradiated at
341 40kGy) and ketogenic diet (S0382-E210, ssniff Spezialdiäten, irradiated at 25kGy) or on control diet
342 (MD.230304, Envigo, irradiated at 25kGy) and stearate-supplemented diet (MD.230306, Envigo, irradiated
343 at 25kGy). The animals were maintained under standard habitat conditions (humidity: 40–70%,
344 temperature: 22°C) with a 12:12 light cycle.

345

346 *Stool preparation for fecal/cecal microbial transplant*

347 Single human stool samples and single mouse cecal contents were suspended in a 20% glycerol
348 PBS solution at 10mg of stool per mL. For the mix of five healthy donor stools (5HD), equal volumes of
349 each single suspension were mixed.

350

351 *Inflammatory mouse model of CRC*

352 GF and SPF mice were administered a single intraperitoneal injection of sterile-filtered AOM
353 (Sigma-Aldrich, 10mg/kg mouse body weight). SPF mice were administered a sterile-filtered antibiotic mix

354 (vancomycin hydrochloride (Sigma-Aldrich, 500mg/L), ampicillin (Sigma-Aldrich, 1g/L), neomycin (Sigma-
355 Aldrich, 1g/L) and metronidazole (Sigma-Aldrich, 1g/L)) via their drinking water for one week prior to AOM
356 injection. Microbiomes were replaced with donor microbiomes via oral gavage. Mice were administered
357 a total of three cycles of DSS, with a two-week-long recovery period between each cycle. DSS was
358 refreshed mid-cycle. Half of the mice were randomly allocated to each dietary condition at the end of the
359 last cycle of DSS. Further details regarding the experimental setups can be found in Supplementary Table
360 9.
361
362 *Long-term lowly-inflammatory mouse model of CRC*
363 GF mice were administered four intraperitoneal injections of sterile-filtered AOM (Sigma-Aldrich,
364 15mg/kg mouse body weight), once per week for four weeks and received donor microbiomes via oral
365 gavage. Half of the mice were randomly allocated to the ketogenic diet one week after the first injection
366 of AOM. Further details regarding this experimental setup can be found in Supplementary Table 9.
367
368 *Mouse euthanasia*
369 All mice were injected intraperitoneally with ketamine (150mg/kg, Nimatek®, Medikamio) and
370 medetomidine (1mg/kg, Dorbene®, Zoetis) at endpoint and blood was collected from the portal vein
371 followed by cervical dislocation.
372
373 *Colonic tumor burden and tumor size assessment*
374 Colons were resected at endpoint and small portions of the proximal colon were snap-frozen for
375 further downstream analyses. The remaining distal portion of the colon was used for the assessment of
376 tumor burden. Colonic tumors were counted under a Leica Wild M10 microscope and photographed using

377 a Leica MC170HD camera. Colonic tumor surface size was assessed from the photographs using FIJI Image
378 J.
379
380 *Lamina propria immune cell isolation*
381 Colons (opened longitudinally) were cut into 2 cm-long pieces and pre-digested in strip medium
382 (RPMI GlutaMAX® (Gibco), 3%FBS (Lonza), 1%P/S (Gibco), 5mM EDTA (Sigma-Aldrich), 0.154mg/mL DTT
383 (Merck)) in a bacterial shaker at 800rpm, 37°C for 20 minutes. After incubation, the strip medium was
384 collected, filtered through a 70µM and retained to further immunophenotyping, constituting the intra-
385 epithelial lymphocyte (IEL) fraction. The remaining intestinal pieces were digested (RPMI GlutaMAX®
386 1%P/S, 5mg/mL Liberase (Merck Life Sciences), 25mg/mL DNase (Sigma-Aldrich)) for 30 minutes at 800
387 rpm, 37°C in a bacterial shaker. The digest was pressed though a 70µM cell strainer, washed with FCS-
388 containing RPMI medium and retained for further immunophenotyping. Alternatively, colons were
389 processed according to the Mouse Lamina Propria Dissociation Kit (Miltenyii) instructions, with the
390 following modifications: 1) a bacterial shaker was used (800rpm, 37°C) instead of a MACSmix tube rotator.
391 2) 70µM cell strainers were used instead of 100µm cell strainers.
392
393 *Spleen and mesenteric lymph node immune cell isolation*
394 Spleens were injected with 1mL of RPMI GlutaMAX® 1%P/S, 5mg/mL Liberase (Merck Life
395 Sciences), 25mg/mL DNase (Sigma-Aldrich), cut up into small pieces (<1mm^2) and incubated at 37°C for
396 30 minutes. After incubation, spleens were pressed though a 70µM cell strainer, washed with FCS-
397 containing RPMI medium and retained for further immunophenotyping. MLNs were pressed through a
398 70µM cell strainer without prior enzymatic digestion.
399
400 *Cell counting*

401 The cellular concentration of all cell suspensions was quantified using the Cedex XS Analyzer
402 (Roche), by mixing 10µL of cells with 10µL of Trypan Blue solution (Roche) and loading 10µL into the Cedex
403 Smart Slide (ibidi) channel; or using the CASY Cell Counter and Analyzer (OMNI Life Sciences), by diluting
404 10µL of cell suspension in 10mL of CASYton (OMNI Life Sciences) solution.
405
406 *Immune cell restimulation*
407 Cell suspensions obtained from colons, spleens and MLNs were distributed in a 96-well plate and
408 either directly stained or restimulated prior to intracellular cytokine staining using 50ng/mL PMA (Sigma-
409 Aldrich) and 1.5µg/mL ionomycin (Alfa Aesar) in RPMI GlutaMAX® 10% FBS 1% P/S for four hours at 37°C.
410 Brefeldin A (eBioscience (Invitrogen)) was added after the first hour.
411
412 *Immune cell staining and acquisition (FACS)*
413 Cells were stained with fluorescent extracellular antibody mixes (LIVE/DEAD Fixable Near-Infrared
414 Dead Cell Stain Kit (ThermoFisher Scientific) 1:1000, antibodies 1:100 in FACS buffer) and incubated for
415 30 minutes at 4°C or overnight at 4°C. For the staining of macrophages and dendritic cells, an anti-CD16/32
416 (1:50) antibody was used to block unspecific binding prior to staining with fluorescent antibodies. After
417 incubation, cells were washed, then fixed and permeabilized using the Cytofix/Cytoperm Kit (BD
418 Biosciences), according to the kit manual. After permeabilization, cells were stained with fluorescent
419 intracellular antibody mixes (antibodies 1:100 in Perm Buffer (from Cytofix/Cytoperm Kit)) and incubated
420 for 30 minutes at 4°C. After incubation, cells were washed and analyzed in a FACS Canto II or on a FACS
421 LSRFortessa Cell Analyzer. All antibodies are listed in Supplementary Table 10. Data analysis was
422 performed using FlowJo and R was used for graphical representation. All gating strategies for immune cell
423 profiling presented in this article can be found in Supp. Fig. 9 and 10.
424

425 *Tissue staining*

426 Liver lobes and portions of colons were included in Tissue Freezing Medium (Leica) and snap-
427 frozen in liquid nitrogen immediately upon collection. Slides were thawed and air dried for 30 minutes a
428 room temperature prior to staining. For Alcian blue staining, 7µm-thick colon cryosections were fixed with
429 10% buffered formalin for 30 minutes. After fixation, slides were washed, incubated in 3% acetic acid (Carl
430 ROTH) for three minutes, then stained with Alcian Blue (Merck) for 30 minutes, then washed and
431 counterstained with Nuclear Fast Red (Merck) for five minutes. For H&E staining, 7µm-thick liver
432 cryosections were fixed in methanol for 10 minutes. Slides were left to dry for two minutes, then stained
433 for one minute in hematoxylin, then washed and stained for three minutes in eosin. Both liver and colon
434 slides were dehydrated in ethanol (80%, 95%, 100%), then stained for five minutes in Neo-Clear® (xylene
435 substitute). For immunofluorescent staining, slides were fixed for 10 minutes in acetone, which was left
436 to evaporate, then blocked with 10% FBS (in PBS) for one hour. Slides were stained overnight with the
437 primary antibody (1:200) at 4°C. Slides were washed with 0.01% Tween-20 (in PBS) the following morning
438 and stained with a secondary antibody (1:220) and DAPI (1:1000) in 1% FBS (in PBS) for an hour at room
439 temperature. Slides were then washed with 0.01% Tween-20 (in PBS). For mounting of slides, 5-6µL of
440 Tissue-tek coverslipping resin were dripped onto each sample and a coverslip was placed on top.

441

442 *ELISA*

443 LPS ELISAs were performed on mouse plasma samples using the ENDONEXT™ EndoELISA®
444 Endotoxin Detection Assay (BioVendor) according to the manufacturers' instructions. Lipocalin-2 was
445 detected in mouse fecal samples using the Mouse Lipocalin-2/NGAL DuoSet ELISA Kit (DY1857-05, R&D
446 Systems) according to the manufacturers' instructions.

447

448 *Sodium acetoacetate synthesis and long-chain fatty acid – albumin complexation*

449 Sodium acetoacetate (NaAcAc) was produced in-house by hydrolysis of an equimolar solution of
450 NaOH (Sigma-Aldrich) with ethyl acetoacetate (Sigma-Aldrich). The mixture was heated to 37°C in a water
451 bath overnight to produce sodium acetoacetate, water, and ethanol. A rotary evaporator with vacuum
452 was used to evaporate out the ethanol and the water and the remaining precipitate was stored at -20°C
453 until use.

454 Stearic acid, oleic acid and lauric acid (Sigma) were solubilized at 80mM in isopropanol (Sigma),
455 by heating to 37°C for ten minutes. Bovine serum albumin (BSA, Carl Roth) was solubilized in cell culture
456 medium at 2%. Pre-warmed dissolved long-chain fatty acids and pre-warmed BSA were mixed at a 1:1
457 ratio and complexed in a water bath at 37°C for an hour. The BSA-long-chain fatty acids and control
458 solutions were filtered through a 0.45µm sterile filter before use.

459 NB: When these products were used for experiments, the indicated concentrations were
460 calculated based on the assumption that all obtained products were pure and all available long-chain fatty
461 acid molecules were complexed to BSA. Thus, the true bio-available concentration of these products
462 remains undetermined, and lower than indicated.

463

464 *Cell culture maintenance*

465 HCT116, HT-29 and Caco-2 CRC cell lines were obtained from ATCC and maintained in DMEM-F12
466 with 10% [v/v] foetal bovine serum (FBS) and 1% [v/v] penicillin/streptomycin. Cell lines were
467 mycoplasma-free and authenticated before their use in this study (STR analysis, DSMZ).

468

469 *T cell differentiation assay*

470 Spleens and lymph nodes from young (<8-week-old) male and female C57BL/6J mice were
471 isolated using the CD4^{+} T Cell Isolation Kit (Miltenyii Biotec) according to the manufacturer's instructions.
472 Single cell suspensions were counted using a Neubauer improved counting chamber (VWR). 200 000 cells

473 per well were dropped onto a 96-well plate pre-coated with anti-CD3 at 5ug/mL per well (incubated for
474 at least three hours at 37°C) and preloaded with a Th17 cell differentiation cytokine mix (final
475 concentrations: 2ng/mL TGF-β (R&D systems), 30ng/mL IL-6 (Miltenyii Biotec), 5µg/mL anti-IFNγ and
476 1µg/mL anti-CD28) and with the treatments of interest at the concentrations indicated in each figure.
477 Three days later, cells were restimulated, stained and analyzed as described above.
478
479 *Proliferation assays*
480 For the evaluation of dose-dependent responses to stearic acid, 3000 HCT116, HT-29 and Caco-2
481 cells were seeded per well in a 96-well plate and were treated with the indicated concentrations of BSA-
482 stearate or a matching control containing cell culture medium, BSA and isopropanol. Confluence was
483 monitored with the IncuCyte imaging system (Sartorius). The IncuCyte ZOOM software (2018B, Sartorius)
484 was used to create a mask for confluence detection.
485 For the evaluation of the effect of different long-chain fatty acids on tumor cell growth, 6500 HT-
486 29 cells were seeded per well in a 96-well plate. 24 hours after seeding, cells were treated with BSA-
487 stearate, BSA-oleate and BSA-laurate at the indicated concentrations or an equal volume of DMSO as
488 control for 48 hours, in the presence or absence of the caspase inhibitor zVAD (Z-VAD-FMK, InVivoGen).
489 Staurosporine (81590-10, SanBio), a protein kinase C inhibitor, was used as a positive control. Wells were
490 imaged using Cytation10 every 24h and cell viability was assessed using CellTiterGlo (G9241, Promega)
491 72h after treatment according to the user manual.
492
493 *RNA isolation from murine tissues and Quantitative Polymerase Chain Reaction (qPCR)*
494 RNA was isolated from mouse tissue samples using the Machery-Nagel Nucleospin RNA Isolation
495 Kit (ThermoFischer Scientific), following the kit manual, after tissue homogenization by bead-beating in

496 the TissueLyzerII (Qiagen) for five minutes, at 40Hz. The concentrations and purities of the extracted RNA
497 samples were measured using a Nanodrop 2000 spectrophotometer.
498 cDNA was obtained by reverse transcription using the High-Capacity cDNA Reverse Transcription
499 Kit (Applied Biosystems, Thermofisher Scientific). The Absolute Blue qPCR SYBR Green Low ROX Kit
500 (ThermoFisher Scientific) was used for the amplification. 125nM of each primer (primer sequences can be
501 found in Supplementary Table 11) and 50 ng of cDNA was used per reaction and run on a 7500 FAST Real
502 time PCR Detection System cycler (Applied Biosciences) set to 95°C for 15 minutes, followed by 40 cycles
503 of 95°C for 30 seconds, 60°C for 30 seconds and 72°C for 30 seconds. Expression levels of the genes of
504 interest were normalized against the reference genes β-actin and GAPDH using the qbase+ software, in
505 accordance with the MIQE guidelines[48].
506
507 *RNA extraction from cell pellets and sequencing*
508 RNA was extracted from treated cell pellets using the miRNeasy Mini Kit (#74106, Qiagen). DNA
509 was digested using RNase-free DNase (RNase-free DNase Set, #79256, Qiagen). For library preparation,
510 1 µg of RNA was poly(A) selected, fragmented and reverse transcribed by using the Elute, Prime, Fragment
511 Mix (Illumina). 1 µg of RNA was poly(A) selected and fragmented by using the Elute, Prime, Fragment Mix
512 (Illumina). Reverse transcription, End repair and adaptor ligation and library enrichment were performed
513 as described in the Low Throughput protocol of the TruSeq RNA Sample Prep Guide. RNA library quantity
514 and quality were assessed with the Fragment Analyzer (Agilent). RNA libraries were sequenced as 50 bp
515 paired-end on Illumina NextSeq2000 sequencer at the LCSB genomics platform (RRID: SCR_021931).
516
517 *RNA data processing and analysis*
518 FastQ files were processed using a snakemake workflow which can be found here:
519 https://gitlab.lcsb.uni.lu/aurelien.ginolhac/snakemake-rna-seq. Tag version: 0.5.4. Container software

520 set: https://hub.docker.com/r/ginolhac/snake-rna-seq tag 0.8. Briefly, reads were trimmed with
521 AdaptorRemoval with a minimum length of the remaining reads set to 35 bp (version 2.3.3[49,50]). Trimmed
522 reads were mapped to human reference genome GRCh38 (from Ensembl release 102) using STAR
523 v2.7.11a[51]. Quality control was performed using fastqc (version 0.12.1) and fastq Screen (version 0.15.3[52])
524 and summarized using multiqc (version 1.17). Read counts were extracted using Rsubread::featureCounts
525 v2.16.0[53] and reads with counts below 10 were removed prior to differential expression analysis using
526 DESeq2 version 1.42.0 with apeglm to preserve large log2-fold changes v1.24.0[54]. The identified batch
527 effect (biological replicate) was removed using ComBat-Seq implemented in the R package sva[55] and
528 differential gene expression analysis performed using DESEq2[56]. Log 2 fold change values were shrunken
529 using ashr[57]. Genes were pre-ranked by the log 2 fold-change values and geneset enrichment analyses
530 performed using the GSEA() function implemented in the clusterProfiler R package. Hallmark genesets
531 were retrieved using the msigdbr R package and the Chen et al. genesets[58]. Heatmaps were rendered
532 using the ComplexHeatmap R package. TCGA COAD and READ data (data release v36) were retrieved from
533 the GDC portal and the expression data from patients providing paired distant normal and primary tumor
534 samples filtered out (n = 50 patients). Geneset expression scores for TCGA and our in-house RNA-Seq
535 dataset were calculated using the R package singscore[59,60] and TPM expression values. Scripts can be
536 found: https://gitlab.com/uniluxembourg/fstm/dlsm/mdm.
537
538 *DNA isolation from fecal samples (mouse, human)*
539 Fecal DNA was isolated using the DNeasy PowerSoil DNA Isolation Kit (Qiagen), according to the
540 kit manual, but with the following modification - the sample was homogenized using the TissueLyzerII for
541 five minutes at 40Hz instead of by vortexing. DNA extracted from human fecal samples was additionally
542 subjected to processing through the DNA Clean and Concentrator Kit (Zymo Research). The concentrations
543 and purities of the extracted DNA samples were measured using a Nanodrop 2000 spectrophotometer.

544

545 *16S rRNA amplicon sequencing and WGS*

546 For 16S rRNA sequencing, 5 ng of DNA extracted from human or mouse fecal samples was
547 subjected to amplicon sequencing of the V4 region of 16S rRNA genes using primers 515F and 805R
548 (primer sequences can be found in Supplementary Table 11). Samples with low microbial biomass were
549 excluded. Sequencing was performed on a MiSeq instrument (Illumina) using 2×300 base pair read
550 lengths.

551 For WGS, 200 ng of DNA extracted from human fecal samples was used for metagenomic library
552 preparation using the Next Generation Sequencing DNA Library Prep Kit (Westburg), according to the user
553 manual. 100 ng of DNA extracted from mouse fecal samples was used for metagenomic library
554 preparation using the FX DNA Library Kit (Qiagen), according to the user manual. The average insert size
555 of libraries was 450 base pairs for human fecal samples and 530 base pairs for mouse fecal samples.
556 Sequencing was performed on a NextSeq500 (Illumina, for human fecal samples) or on a NextSeq2000
557 (Illumina, for mouse fecal samples) instrument using 2×150 base pair read lengths.

558 All prepared libraries were quantified using the Qubit® dsDNA BR Assay Kit (Thermofisher
559 Scientific) and Qubit® 3 Fluorometer (ThermoFisher Scientific) and sample quality was assessed using the
560 Bioanalyzer High Sensitivity DNA Analysis Kit (Agilent Technologies).

561

562 *16S data analysis*

563 Raw 16S rRNA gene sequences (FASTAQ files) were cleaned, processed and merged up to an
564 amplicon sequence variant (ASV) count table using the DADA2 pipeline[61]. SILVA train sets (versions 132
565 (engraftment of 5HD mix in mice) to 138 (community changes over time)) were used for taxonomy
566 inference. Samples with no reads, ASVs with no identified phylum or class and taxa present in less than
567 5% of samples were excluded where necessary. Data was aggregated to genus level and relative

568 abundances were computed, or centered log-ratio (CLR) transformation[62] was performed. Differential
569 analysis and graphical representation were performed in R, using the packages from Bioconductor
570 (DESeq2[63,64], phyloseq[65]) and tidyverse (ggplot). Details on the workflows and scripts can be found on
571 https://gitlab.com/uniluxembourg/fstm/dlsm/mdm.
572
573 *WGS data analysis for human fecal samples*
574 Raw genome sequences (FASTQ files) were cleaned using the Sunbeam pipeline[66]. Function
575 profiling was performed with HUMAnN Version 3.0[67] using the quality-controlled and host-
576 decontaminated FASTQ files obtained from Sunbeam. Graphical representation was performed in R, using
577 the packages from tidyverse, broom and RColorBrewer.
578
579 *WGS data analysis for mouse fecal samples*
580 The Integrated Meta-omic Pipeline (IMP; v3 - commitID #6f1badf7)[68] was used to process paired
581 forward and reverse reads using the built-in metagenomic workflow. The workflow includes pre-
582 processing, assembly, genome reconstruction and functional annotation of genes based on custom
583 databases in a reproducible manner. *De novo* assembly was performed using the MEGAHIT (version 2.0)
584 assembler. Default IMP parameters were retained for all samples. MetaBAT2 and MaxBin2 in addition to
585 binny[69] were used for binning and genome reconstructions, i.e. MAGs. Subsequently, a non-redundant
586 set of MAGs was obtained using DASTool v1.1.461 with a score threshold of 0.7 for downstream analyses,
587 and those with a minimum completion of 90% and less than 5% contamination as assessed by CheckM
588 v1.1.3. Taxonomy was assigned to the MAGs using the extensive database packaged with gtdbtk v2.0.1.
589 In addition, Kraken2 implemented in IMP was used for taxonomic assignment of reads. For the analyses
590 of functional potential from the assembled contigs, open-reading frames were predicted from contigs
591 using a modified version of Prokka that includes Prodigal gene predictions for complete and incomplete

592 open-reading frames. The identified genes were annotated with a hidden Markov models (HMM)
593 approach, trained using an in-house database including KOs derived from the Kyoto Encyclopedia of Genes
594 and Genomes (KEGG) database[70–72].
595 Differential analysis was performed using the package DESeq2[56] and using Wilcoxon rank sum test
596 performed on CLR-transformed Kraken2 reads counts. Non-metric dimensional scaling (NMDS) analyses
597 were performed on robust Aitchison distances calculated from Kraken2 read counts using the R package
598 *vegan* (version 2.6-6.1). For further analysis as well as graphical representation R packages *ggplot2*,
599 *ggpubr* (version 0.6.0), *tidyverse, gghx4* and *RColorBrewer* (version 1.1-3) were used. Details on the
600 workflows and scripts can be found on https://gitlab.com/uniluxembourg/fstm/dlsm/mdm.
601
602 *Human fecal sample and mouse fecal pellet homogenization for metabolite extraction*
603 Circa 1g of frozen human fecal material was milled in a cryogenic grinder (6875D Freezer/Mill®,
604 SPEX® SamplePrep, Instrument Solutions) reducing the samples to a fine powder. Homogenized fecal
605 powders were resuspended in 500µL of MilliQ® water, then centrifuged at maximum speed.
606 MilliQ® water was added to mouse fecal pellets at a 1:16 dry weight to water ratio, in tubes
607 containing ceramic homogenization beads. Samples were homogenized at 6000rpm, for two 30-second-
608 long cycles at 4°C, in a Precellys®24 Homogenizer (Bertin Corp.), incubated at 4°C for ten minutes, then
609 centrifuged at maximum speed.
610 Supernatants were collected for further downstream processing.
611
612 *Metabolite extraction*
613 An internal standard mix (ISM) was added to the samples (human fecal samples, murine fecal
614 samples and murine plasma samples) and proteins were precipitated. Proteins were pelleted,
615 supernatants were collected and phospholipids were removed (for HILIC LC-MS). Phase separation was

616 achieved by addition of chloroform, aliquots of the polar and non-polar phase were transferred into GC-
617 MS vials and solvents were evaporated in a rotary vacuum evaporator at 4°C overnight. Dried samples
618 were then reconstituted for analysis.

619 Hydrophilic interaction chromatography (HILIC) was done on a Thermo Q Exactive HF mass
620 spectrometer (ThermoFisher Scientific) equipped with SeQuant ZIC-pHILIC 20x2.1mm columns (Merck
621 Millipore) using 20mM AmAc in water as mobile phase A and 20mM AmAc in 90% ACN + 0.1% formic acid
622 as mobile phase B.

623 For untargeted GC-MS of murine plasma samples, metabolite derivatization was performed using
624 a multi-purpose sampler (Gerstel) and data were acquired on 7890B GC (Agilent Technologies) coupled to
625 a 5977A mass selective detector (MSD, Agilent Technologies) or Vanquish UHPLC (ThermoFisher
626 Scientific), coupled to a Q Exactive HF mass spectrometer (ThermoFisher Scientific).

627 Details regarding sample processing and acquisition are provided in Supplementary File 1.

628

629 *Metabolite extraction from murine fecal samples for short-chain fatty acid (SCFA) quantification*

630 For targeted and absolute quantitative SCFA detection in mouse fecal samples, derivatization was
631 performed in the organic phase using diethyl ether (VWR). A dilution series of a volatile free acid mix
632 (VFAM, Supelco®, Sigma-Aldrich) and separate quality control samples were prepared. Internal standard
633 (IS) of 10mM 2-ethylbutyric acid (Sigma-Aldrich) in methanol, MilliQ® water and 18.5% hydrochloric acid
634 (Sigma-Aldrich) were added to all samples. After 15 minutes of agitation at 15°C in the Thermomixer
635 (Eppendorf), two subsequent 99% diethyl ether extractions were performed. The decanted supernatants
636 were pooled, then aliquoted in triplicates and N-Methyl-N-(tert-butyldimethylsilyltrifluoro acetamide)
637 w/1% tert butyldimethylchlorosilane (MTBSTFA, Interscience) was added for analysis. The samples were
638 analyzed on an 8890 GC (Agilent Technologies), coupled to an 5977B MSD (Agilent Technologies).

639 Details regarding sample processing and acquisition are provided in Supplementary File 1.

640

641 *Murine plasma bile acid (BA) quantification by ultra-high performance liquid chromatography – tandem*
642 *mass spectrometry (UHPLC-MS/MS)*

643 10 µL of plasma were used for bile acid (BA) quantification. BAs were analysed using UHPLC-
644 MS/MS, consisting of an ExionLC (Sciex) coupled to a QTrap 5500 mass spectrometer (Sciex). Electrospray
645 ionization was performed in the negative ionization mode. Chromatographic separation was run on an
646 ethylene bridged hybrid (BEH) C18 column (2.1x100 mm, 1.7µm, ThermoFisher Scientific). The mobile
647 phase consisted of water, containing 0.1% formic acid and 5mM ammonium acetate or acetonitrile (ACN,
648 Carl ROTH). The analytes were separated by a gradient elution. BA detection was performed in the
649 multiple reaction monitoring (MRM) mode. Standards for all shown BAs, as well as the deuterated BA
650 internal standard (IS) substances d4-CA, d4-GCA and d4-TCA were purchased from Sigma-Aldrich Chemie
651 GmbH (Taufkirchen, Germany), Avanti Polar Lipid (Alabaster, USA) and Steraloids (Newport, USA). Further
652 details can be found in García-Cañaveras et al., 2012[73] and in Supplementary File 1.

653

654 *Metabolomic profiling data pre-processing of untargeted LC-MS datasets*

655 Raw data files obtained through LC-MS of human stool and murine plasma and stool samples were
656 processed in TraceFinder (version 5.1.203.0) for peak identification and annotation. Three different in-
657 house libraries, generated with reference standards, as well as one commercially available library,
658 mzCloud Offline for mzVault 2.3_Omics_2020A.db, in the Advanced Mass Spectral Database (AMSD)
659 (HighChem, from ThermoFischer Scientific), were used for peak annotation, with the adduct formulas
660 $[M+H]^+$ and $[M-H]^-$. Annotated features and integration tables were exported for post-processing.

661

662 *Metabolomic profiling data pre-processing of untargeted GC-MS datasets*

663 Raw data files obtained through GC-MS murine plasma and stool samples were processed in
664 MetaboliteDetector[74] (version 3. 220190704) for peak identification and annotation. An in-house library,
665 generated with reference standards was used for peak annotation. Deconvolution settings were applied
666 as follows: peak threshold = 5, minimum peak height = 5, bins per scan = 10, deconvolution width = 5
667 scans, no baseline adjustment, minimum 15 peaks per spectrum and no minimum required base peak
668 intensity. The data was normalized using the response ratio of the integrated peak area of each metabolite
669 and the integrated peak area of the IS, as described in[75]. Annotated features and integration tables were
670 exported for post-processing.
671
672 *Metabolomic profiling post-processing data analysis*
673 For murine plasma metabolites identified in the SPF experiment, data was manually curated
674 based on the pooled sample, spiked with the ISM. Features, which could not be confirmed through MS2
675 data (from the commercially available database[76]) or through the ISM were filtered out. Metabolites with
676 missing (N/A) values were also filtered out. Single metabolite intensities were normalized to the total
677 metabolite area and corrected using the mean value of total metabolite values from all samples. LC-MS
678 and GC-MS data were unified, and duplicate metabolites were filtered out, based on reliability and
679 consistency of the peak areas.
680 Human stool sample data was similarly processed (but without the element of data unification
681 between methods).
682 For murine plasma metabolites identified in the GF experiment (GC-MS), metabolites with missing
683 (N/A) values were filtered out.
684 Murine stool SCFA content was quantified based on an IS and using the MassHunter Quantitative
685 Analysis Software (version 10.2.733.8). In the LC-MS and GC-MS datasets, metabolites with over 20%
686 missing (N/A) values were filtered out. Data from murine stool untargeted LC-MS, GC-MS and SCFA

687 quantification was unified and duplicate metabolites were filtered out, based on reliability and
688 consistency of the peak areas.

689 Univariate statistical analysis with Benjamini-Hochberg false discovery rate (BH FDR, performed
690 for all datasets), principal component analysis (PCA), scaling, centering and graphical representation in
691 the form of a heatmap (ComplexHeatmap R package[77]) or log2foldchanges were performed in R version
692 4.2.1 and Rstudio version 1.4.1717. For data scaling and centering, the standard deviation was set to a
693 value of 1 and the mean value was set to 0.

694

695 Total and free fatty acid extraction

696 Powders of mouse diet samples were prepared by placing samples in 7 mL Precellys® tubes (VWR)
697 containing 10 steel beads and homogenization at 9000 rpm for 3 cycles of 30 seconds at 4°C to. For
698 extraction of total and free fatty acids mouse diet powders and mouse fecal samples were homogenized
699 in Precellys® tubes (VWR) containing 600 mg ceramic beads and MeOH + ISM (final concentration 2 µg/ml)
700 in a sample to weight ration of 1:30. Non-polar fatty acids were extracted using methyl-tert-butyl ether
701 (MTBE) and H_2O to induce phase separation. For quantification of free fatty acids, aliquots of the non-
702 polar phase were transferred into glass vials, solvents were evaporated, and samples were kept until data
703 acquisition. For quantification of total fatty acids, dried non-polar extracts were dissolved in isopropanol
704 and 0.4 M NaOH was added to perform alkaline hydrolysis. After incubation for 30 min at 37°C, samples
705 were acidified with 2 M HCl and fatty acids were extracted using hexane.

706 Plasma fatty acids were extracted from 8 µl mouse plasma mixed with ACN/H_2O (4+1) + ISM (final
707 concentration 2 µg/ml) using the same workflow with the exception that an acidic hydrolysis was
708 performed prior phase separation using 5 M HCl.

709 Dried total fatty acid extracts were reconstituted, filtered using Phenex-PTFE syringe filters and
710 analyzed on an Agilent 1290 LC coupled to an Agilent 6560 Q-TOF MS system equipped with a Dual Agilent

711 Jet Stream ESI source using Agilent Mass Hunter LC/MS Data Acquisition (version B.09.00, Build
712 9.0.9044.0) for data acquisition.
713 Details regarding sample processing and acquisition are provided in Supplementary File 1.
714
715 Pre-processing of total and free fatty acid datasets
716 Raw data obtained through fatty acid LC-MS profiling were processed in Agilent Mass Hunter
717 Profinder (ver 10.0 SP1, Build 10.0.10142.1). Target compounds were identified by exact mass (mass error
718 ±5 ppm), isotopic pattern and retention time (±0.15 min) matching (Batch Targeted Feature Extraction).
719 Semi-quantification was based on integrated peak area of the deprotonated target compound and
720 normalization to internal standards.
721
722 *Other data analyses*
723 All other data analysis, statistical analysis, and graphical representation, which is not described in
724 the above sections, was performed using Graphpad Prism version 9.4.1.
725
726 *Data availability*
727 Raw sequencing data files for 16S gene sequencing from murine fecal samples are available at the
728 ENA's sequence archive under the accession PRJEB70917 (GF) and PRJEB70920 (SPF). Raw sequencing
729 data files for 16S gene sequencing from human stool samples are available at the ENA's sequence archive
730 under the accession PRJEB70932. Raw sequencing data samples for mouse stool samples are available at
731 the ENA's sequence archive under the accession PRJEB66281. Raw sequencing data files for WGS from
732 human stool samples are available at the ENA's sequence archive under the accession PRJEB70909. Raw
733 sequencing data files for RNAseq from LCFA-treated HT29 cells can be accessed under ArrayExpress
734 accession number E-MTAB-14429.

735 Data used to generate the figures are also provided as a 'Source Data' file. Source data are
736 provided with this paper.
737
738 **References**

739 1. Colorectal cancer statistics. *WCRF International* https://www.wcrf.org/cancer-trends/colorectal-
740 cancer-statistics/.
741 2. Akimoto, N. *et al.* Rising incidence of early-onset colorectal cancer - a call to action. *Nat. Rev. Clin.*
742 *Oncol.* **18**, 230–243 (2021).
743 3. Weber, D. D. *et al.* Ketogenic diet in the treatment of cancer – Where do we stand? *Mol. Metab.* **33**,
744 102–121 (2019).
745 4. Dmitrieva-Posocco, O. *et al.* β-Hydroxybutyrate suppresses colorectal cancer. *Nature* **605**, 160–165
746 (2022).
747 5. Ang, Q. Y. *et al.* Ketogenic Diets Alter the Gut Microbiome Resulting in Decreased Intestinal Th17
748 Cells. *Cell* **181**, 1263-1275.e16 (2020).
749 6. Kong, C. *et al.* Ketogenic diet alleviates colitis by reduction of colonic group 3 innate lymphoid cells
750 through altering gut microbiome. *Signal Transduct. Target. Ther.* **6**, 154 (2021).
751 7. Wei, R. *et al.* Ketogenesis Attenuates KLF5-Dependent Production of CXCL12 to Overcome the
752 Immunosuppressive Tumor Microenvironment in Colorectal Cancer. *Cancer Res.* **82**, 1575–1588
753 (2022).
754 8. Ferrere, G. *et al.* Ketogenic diet and ketone bodies enhance the anticancer effects of PD-1 blockade.
755 *JCI Insight* **6**, 145207 (2021).
756 9. Wong, C. C. & Yu, J. Gut microbiota in colorectal cancer development and therapy. *Nat. Rev. Clin.*
757 *Oncol.* **20**, 429–452 (2023).

758 10. El Tekle, G. & Garrett, W. S. Bacteria in cancer initiation, promotion and progression. *Nat. Rev.*
759 *Cancer* **23**, 600–618 (2023).
760 11. Paoli, A. *et al.* Ketogenic Diet and Microbiota: Friends or Enemies? *Genes* **10**, 534 (2019).
761 12. Hyun, Y. S. *et al.* Role of IL-17A in the development of colitis-associated cancer. *Carcinogenesis* **33**,
762 931–936 (2012).
763 13. Cairo, C. & Webb, T. J. Effective Barriers: The Role of NKT Cells and Innate Lymphoid Cells in the Gut.
764 *J. Immunol. Baltim. Md 1950* **208**, 235–246 (2022).
765 14. Jukic, A., Bakiri, L., Wagner, E. F., Tilg, H. & Adolph, T. E. Calprotectin: from biomarker to biological
766 function. *Gut* **70**, 1978–1988 (2021).
767 15. Mu, C. *et al.* Probiotics counteract hepatic steatosis caused by ketogenic diet and upregulate AMPK
768 signaling in a model of infantile epilepsy. *EBioMedicine* **76**, 103838 (2022).
769 16. Nan, F. *et al.* Mannose: A Sweet Option in the Treatment of Cancer and Inflammation. *Front.*
770 *Pharmacol.* **13**, (2022).
771 17. Gonzalez, P. S. *et al.* Mannose impairs tumour growth and enhances chemotherapy. *Nature* **563**,
772 719–723 (2018).
773 18. Liu, Q., Li, X., Zhang, H. & Li, H. Mannose Attenuates Colitis-Associated Colorectal Tumorigenesis by
774 Targeting Tumor-Associated Macrophages. *J. Cancer Prev.* **27**, 31–41 (2022).
775 19. De Simone, V., Pallone, F., Monteleone, G. & Stolfi, C. Role of TH17 cytokines in the control of
776 colorectal cancer. *Oncoimmunology* **2**, e26617 (2013).
777 20. Ternes, D. *et al.* Microbiome in Colorectal Cancer: How to Get from Meta-omics to Mechanism?
778 *Trends Microbiol.* **28**, 401–423 (2020).
779 21. Parker, B. J., Wearsch, P. A., Veloo, A. C. M. & Rodriguez-Palacios, A. The Genus Alistipes: Gut
780 Bacteria With Emerging Implications to Inflammation, Cancer, and Mental Health. *Front. Immunol.*
781 **11**, 906 (2020).

782 22. Sohlenkamp, C. & Geiger, O. Bacterial membrane lipids: diversity in structures and pathways. *FEMS*
783 *Microbiol. Rev.* **40**, 133–159 (2016).
784 23. Caswell, B. T. *et al.* Thioesterase enzyme families: Functions, structures, and mechanisms. *Protein*
785 *Sci.* **31**, 652–676 (2022).
786 24. Han, S. *et al.* A metabolomics pipeline for mechanistic interrogation of the gut microbiome. *Nature*
787 **595**, 415–420 (2021).
788 25. Gopalakrishnan, V. *et al.* Gut microbiome modulates response to anti-PD-1 immunotherapy in
789 melanoma patients. *Science* **359**, 97–103 (2018).
790 26. Matson, V. *et al.* The commensal microbiome is associated with anti-PD-1 efficacy in metastatic
791 melanoma patients. *Science* **359**, 104–108 (2018).
792 27. Routy, B. *et al.* Gut microbiome influences efficacy of PD-1-based immunotherapy against epithelial
793 tumors. *Science* **359**, 91–97 (2018).
794 28. Zhang, Y. *et al.* Altered gut microbiome composition in children with refractory epilepsy after
795 ketogenic diet. *Epilepsy Res.* **145**, 163–168 (2018).
796 29. Olson, C. A. *et al.* The Gut Microbiota Mediates the Anti-Seizure Effects of the Ketogenic Diet. *Cell*
797 **173**, 1728-1741.e13 (2018).
798 30. cis-Encoded Small RNAs, a Conserved Mechanism for Repression of Polysaccharide Utilization in
799 Bacteroides | Journal of Bacteriology. https://journals.asm.org/doi/10.1128/jb.00381-16.
800 31. Pudlo, N. A. *et al.* Symbiotic Human Gut Bacteria with Variable Metabolic Priorities for Host Mucosal
801 Glycans. *mBio* **6**, 10.1128/mbio.01282-15 (2015).
802 32. Milani, C. *et al.* Bifidobacteria exhibit social behavior through carbohydrate resource sharing in the
803 gut. *Sci. Rep.* **5**, 15782 (2015).
804 33. Brown, E. M., Clardy, J. & Xavier, R. J. Gut microbiome lipid metabolism and its impact on host
805 physiology. *Cell Host Microbe* **31**, 173–186 (2023).

806 34. Yamada, S. *et al.* Gut microbiota-mediated generation of saturated fatty acids elicits inflammation in
807 the liver in murine high-fat diet-induced steatohepatitis. *BMC Gastroenterol.* **17**, 136 (2017).
808 35. Guillou, H., Zadravec, D., Martin, P. G. P. & Jacobsson, A. The key roles of elongases and desaturases
809 in mammalian fatty acid metabolism: Insights from transgenic mice. *Prog. Lipid Res.* **49**, 186–199
810 (2010).
811 36. Kim, K. S. *et al.* Genome-wide multi-omics analysis reveals the nutrient-dependent metabolic
812 features of mucin-degrading gut bacteria. *Gut Microbes* **15**, 2221811 (2023).
813 37. Flowers, M. T. & Ntambi, J. M. Role of stearoyl-coenzyme A desaturase in regulating lipid
814 metabolism. *Curr. Opin. Lipidol.* **19**, 248–256 (2008).
815 38. Lien, E. C. *et al.* Low glycaemic diets alter lipid metabolism to influence tumour growth. *Nature* **599**,
816 302–307 (2021).
817 39. Zhou, X. *et al.* Stearoyl-CoA Desaturase-Mediated Monounsaturated Fatty Acid Availability Supports
818 Humoral Immunity. *Cell Rep.* **34**, (2021).
819 40. Grajchen, E. *et al.* Fatty acid desaturation by stearoyl-CoA desaturase-1 controls regulatory T cell
820 differentiation and autoimmunity. *Cell. Mol. Immunol.* **20**, 666–679 (2023).
821 41. Kindt, A. *et al.* The gut microbiota promotes hepatic fatty acid desaturation and elongation in mice.
822 *Nat. Commun.* **9**, 3760 (2018).
823 42. McKain, N., Shingfield, K. J. & Wallace, R. J. Metabolism of conjugated linoleic acids and 18 : 1 fatty
824 acids by ruminal bacteria: products and mechanisms. *Microbiology* **156**, 579–588 (2010).
825 43. Yao, J. & Rock, C. O. Exogenous fatty acid metabolism in bacteria. *Biochimie* **141**, 30–39 (2017).
826 44. Fermor, B. F. *et al.* Fatty acid composition of normal and malignant cells and cytotoxicity of stearic,
827 oleic and sterculic acids in vitro. *Eur. J. Cancer Oxf. Engl. 1990* **28A**, 1143–1147 (1992).
828 45. Habib, N. A. *et al.* Stearic acid and carcinogenesis. *Br. J. Cancer* **56**, 455–458 (1987).

829 46. Evans, L. M., Cowey, S. L., Siegal, G. P. & Hardy, R. W. Stearate preferentially induces apoptosis in
830 human breast cancer cells. *Nutr. Cancer* **61**, 746–753 (2009).
831 47. Mitchel, J. *et al.* Computational Identification of Stearic Acid as a Potential PDK1 Inhibitor and In
832 Vitro Validation of Stearic Acid as Colon Cancer Therapeutic in Combination with 5-Fluorouracil.
833 *Cancer Inform.* **20**, 11769351211065979 (2021).
834 48. Bustin, S. A. *et al.* The MIQE guidelines: minimum information for publication of quantitative real-
835 time PCR experiments. *Clin. Chem.* **55**, 611–622 (2009).
836 49. Lindgreen, S. AdapterRemoval: easy cleaning of next-generation sequencing reads. *BMC Res. Notes*
837 **5**, 337 (2012).
838 50. Schubert, M., Lindgreen, S. & Orlando, L. AdapterRemoval v2: rapid adapter trimming,
839 identification, and read merging. *BMC Res. Notes* **9**, 88 (2016).
840 51. Dobin, A. *et al.* STAR: ultrafast universal RNA-seq aligner. *Bioinformatics* **29**, 15–21 (2013).
841 52. Wingett, S. W. & Andrews, S. FastQ Screen: A tool for multi-genome mapping and quality control.
842 *F1000Research* **7**, 1338 (2018).
843 53. Liao, Y., Smyth, G. K. & Shi, W. featureCounts: an efficient general purpose program for assigning
844 sequence reads to genomic features. *Bioinformatics* **30**, 923–930 (2014).
845 54. Zhu, A., Ibrahim, J. G. & Love, M. I. Heavy-tailed prior distributions for sequence count data:
846 removing the noise and preserving large differences. *Bioinformatics* **35**, 2084–2092 (2019).
847 55. Leek, J. T., Johnson, W. E., Parker, H. S., Jaffe, A. E. & Storey, J. D. The sva package for removing
848 batch effects and other unwanted variation in high-throughput experiments. *Bioinformatics* **28**,
849 882–883 (2012).
850 56. Love, M. I., Huber, W. & Anders, S. Moderated estimation of fold change and dispersion for RNA-seq
851 data with DESeq2. *Genome Biol.* **15**, 550 (2014).

852 57. Stephens, M. *et al.* ashr: Methods for Adaptive Shrinkage, using Empirical Bayes. 2.2-63
853 https://doi.org/10.32614/CRAN.package.ashr (2016).
854 58. Chen, Z., Chen, C., Li, L., Zhang, T. & Wang, X. The spliceosome pathway activity correlates with
855 reduced anti-tumor immunity and immunotherapy response, and unfavorable clinical outcomes in
856 pan-cancer. *Comput. Struct. Biotechnol. J.* **19**, 5428–5442 (2021).
857 59. Foroutan, M. *et al.* Single sample scoring of molecular phenotypes. *BMC Bioinformatics* **19**, 404
858 (2018).
859 60. Bhuva, D. D., Cursons, J. & Davis, M. J. Stable gene expression for normalisation and single-sample
860 scoring. *Nucleic Acids Res.* **48**, e113–e113 (2020).
861 61. Callahan, B. J. *et al.* DADA2: High-resolution sample inference from Illumina amplicon data. *Nat.*
862 *Methods* **13**, 581–583 (2016).
863 62. Lin, H. & Peddada, S. D. Analysis of microbial compositions: a review of normalization and
864 differential abundance analysis. *Npj Biofilms Microbiomes* **6**, 1–13 (2020).
865 63. Anders, S. & Huber, W. Differential expression analysis for sequence count data. *Genome Biol.* **11**,
866 R106 (2010).
867 64. Love, M. I., Huber, W. & Anders, S. Moderated estimation of fold change and dispersion for RNA-seq
868 data with DESeq2. *Genome Biol.* **15**, 550 (2014).
869 65. phyloseq: An R Package for Reproducible Interactive Analysis and Graphics of Microbiome Census
870 Data | PLOS ONE. https://journals.plos.org/plosone/article?id=10.1371/journal.pone.0061217.
871 66. Clarke, E. L. *et al.* Sunbeam: an extensible pipeline for analyzing metagenomic sequencing
872 experiments. *Microbiome* **7**, 46 (2019).
873 67. Integrating taxonomic, functional, and strain-level profiling of diverse microbial communities with
874 bioBakery 3 | eLife. https://elifesciences.org/articles/65088.

875 68. Narayanasamy, S. *et al.* IMP: a pipeline for reproducible reference-independent integrated
876 metagenomic and metatranscriptomic analyses. *Genome Biol.* **17**, 260 (2016).
877 69. Hickl, O., Queirós, P., Wilmes, P., May, P. & Heintz-Buschart, A. binny: an automated binning
878 algorithm to recover high-quality genomes from complex metagenomic datasets. *Brief. Bioinform.*
879 **23**, bbac431 (2022).
880 70. Kanehisa, M. & Goto, S. KEGG: Kyoto Encyclopedia of Genes and Genomes. *Nucleic Acids Res.* **28**,
881 27–30 (2000).
882 71. Kanehisa, M. Toward understanding the origin and evolution of cellular organisms. *Protein Sci.* **28**,
883 1947–1951 (2019).
884 72. Kanehisa, M., Furumichi, M., Sato, Y., Kawashima, M. & Ishiguro-Watanabe, M. KEGG for taxonomy-
885 based analysis of pathways and genomes. *Nucleic Acids Res.* **51**, D587–D592 (2023).
886 73. García-Cañaveras, J. C., Donato, M. T., Castell, J. V. & Lahoz, A. Targeted profiling of circulating and
887 hepatic bile acids in human, mouse, and rat using a UPLC-MRM-MS-validated method. *J. Lipid Res.*
888 **53**, 2231–2241 (2012).
889 74. Hiller, K. *et al.* MetaboliteDetector: comprehensive analysis tool for targeted and nontargeted
890 GC/MS based metabolome analysis. *Anal. Chem.* **81**, 3429–3439 (2009).
891 75. De Saedeleer, B. *et al.* Systematic characterization of human gut microbiome-secreted molecules by
892 integrated multi-omics. *ISME Commun.* **1**, 1–6 (2021).
893 76. Xue, J., Guijas, C., Benton, H. P., Warth, B. & Siuzdak, G. METLIN MS2 molecular standards database:
894 a broad chemical and biological resource. *Nat. Methods* **17**, 953–954 (2020).
895 77. Gu, Z., Eils, R. & Schlesner, M. Complex heatmaps reveal patterns and correlations in
896 multidimensional genomic data. *Bioinformatics* **32**, 2847–2849 (2016).

897 78. Varrette, S., Bouvry, P., Cartiaux, H. & Georgatos, F. Management of an academic HPC cluster: The
898 UL experience. in *2014 International Conference on High Performance Computing & Simulation*
899 *(HPCS)* 959–967 (IEEE, Bologna, Italy, 2014). doi:10.1109/HPCSim.2014.6903792.

900

901

902

903 **Figure legends**

904 **Figure 1. Ketogenic diet leads to lower colonic tumor incidence and smaller tumor size in an**
905 **inflammatory model of CRC. | a.** Schematic representation of the dietary AOM/DSS experimental setup
906 in the GF (top) and SPF (bottom) facilities (created with BioRender.com). **b.** Compositions of the KD and
907 SD, with % of calories from the indicated source. **c.** Colonic tumor burden in GF KD- and SD-fed mice. **d-f.**
908 Colonic tumor burden (**d**), normalized average colonic tumor surface area per mouse (**e**) and tumor
909 surface area distribution (small= first tertile, medium=second tertile, big=third tertile; Chi-squared test $\chi 2$
910 (2, N = 87) = 3.4, p = 0.184; **f**) in SPF KD- and SD-fed mice. **g.** Representative images of colons from one
911 KD- and one SD-fed mouse in the SPF facility. Scale bar = 1mm. Data is shown as mean±SD in (**c**), (**d**) and
912 (**e**). Data in (**c**) shows n=6 mice per condition from one experiment. Data in (**d**), (**e**) and (**f**) shows n=8 and
913 9 mice in the KD-fed condition and the SD-fed conditions respectively, pooled from two independent
914 experiments in the SPF facility. Analysis of deviance of a negative-binomial generalized linear model
915 regressing the number of tumors against treatment in (**c**), (**d**). Two-tailed Mann-Whitney U test in (**e**).

916

917 **Figure 2. The tumor-inhibitory effect of ketogenic diet is mediated by the gut microbiome. | a.**
918 Schematic representation of the cecal microbial transfer experimental setup in the GF facility (created
919 with BioRender.com). **b-e.** Colonic tumor burden (**b**), average colonic tumor surface area per mouse (in

920 pixels) (**c**), and tumor surface area distribution (small= first tertile, medium=second tertile, big=third
921 tertile; Chi-squared test $\chi 2$ (2, N = 384) = 10.3, p = 0.00586; **d**), in KC and SC recipient mice. n=16 KC
922 recipient mice and n=13 SC recipient mice. Cecal matter from n=8 different donor mice per condition was
923 used for CMT. Data shown as mean±SD in (**b**) and (**c**). Analysis of deviance of a negative-binomial
924 generalized linear model regressing the number of tumors against treatment in (**b**). Two-tailed Mann
925 Whitney U test in (**c**). **e.** Representative images of the distal portion of the colon from one KC and SC
926 recipient mouse. Scale bar = 1mm.

927

928 **Figure 3. Ketogenic diet alters gut microbiome composition. | a-f.** β-diversity as assessed by PCoA (95%
929 confidence interval) of Bray-Curtis distance in five individual healthy donor stool samples, in a mix of the
930 five healthy donor stool samples (5HD mix) and in murine fecal samples three days after gavage (TG, **a**
931 and **b**); β-diversity as assessed by PCoA (95% confidence interval) of Bray-Curtis distance in murine fecal
932 samples collected over time after diet change (**c** and **d**); Abundance of selected genera which are
933 differentially abundant at at least one time point (using a generalized linear model on CLR, **e** and **f**) in fecal
934 samples collected over time after diet change from SD- and KD-fed mice in the GF (**a**, **c** and **e**) and SPF (**b**,
935 **d**, and **f**) dietary experiments (T0 at diet change, T1-T4 weeks after diet change), as analyzed by 16s rRNA
936 sequencing. **g-i.** β-diversity as assessed by NMDS (95% confidence interval) based on an Aitchison distance
937 matrix (**g**), relative abundance of bacterial families based on Kraken2 IMP output (**h**), and highly
938 characteristic bacterial MAGs (detected in at least six mice in one condition but not more than three mice
939 in the other (diet experiment); detected in at least four mice in one condition but not more than three
940 mice in the other (CMT experiment), **i**) detected in KD, SD, KC and SC murine fecal samples at endpoint,
941 as analyzed by WGS. In (**i**), *Rikenellaceae* are highlighted in light blue and *Muribaculaceae* in dark blue.
942 Data shows n=3 GF SD and n=6 GF KD mice from one experiment in (**a**), (**c**), (**e**), (**g**), (**h**) and (**i**), n=8 SPF KD-

943 fed mice and n=9 SPF SD-fed mice, pooled from two independent experiments in (**b**), (**d**), (**f**), (**g**), (**h**) and
944 (**i**); and n=8 KC and n=8 SC mice from one experiment in (**g**), (**h**) and (**i**).

945

946 **Figure 4. Ketogenic diet alters metabolic profiles, leading to elevated levels of fecal stearate. | a-b.** PCA
947 (95% confidence interval) of identified metabolites from fecal samples from SPF KD- and SD-fed mice (**a**)
948 and from KC and SC recipient mice (**b**), as analyzed by united GC-MS and LC-MS. **c-d.** Scaled free stearic
949 acid levels detected in fecal samples from SPF KD- and SD-fed mice (**c**) and from KC and SC recipient mice
950 (**d**) by LC-MS (polar phase). **e.** Correlation of colonic tumor burden with free fecal stearic acid levels in SPF
951 KD- and SD-fed mice (red) and in KC and SC recipient mice (blue). Two-sided Pearson correlation testing
952 was used. Data shown in (**a**), (**c**), and (**e, red**) are from n=9 SPF SD-fed and n=8 SPF KD-fed mice, pooled
953 from two independent experiments. Data shown in (**b**), (**d**) and (**e, blue**) are from n=8 mice per condition.
954 Data shown as mean±SD, two-sided Mann-Whitney test in (**c**) and (**d**).

955

956 **Figure 5. Stearate is a microbial metabolite. |a**. Schematic representation of type II bacterial fatty acid
957 synthesis created with BioRender, adapted from Yao et Rock (2017)[43]. Core enzymes are shown with their
958 corresponding KEGG orthologs (KOs). Abbreviations: acetyl-CoA carboxylase enzyme complex (AccABCD),
959 β-ketoacyl-ACP synthase 1 (FabB), malonyl-CoA:ACP transacylase (FabD), β-ketoacyl-ACP synthase II
960 (FabF), β-ketoacyl-ACP reductase (FabG), β-ketoacyl-ACP synthase III (FabH), enoyl-ACP reductase enzyme
961 isoforms (FabI, FabK, FabL and FabV), β-hydroxyacyl-ACP dehydratase (FabZ), long-chain-fatty-acid-CoA
962 ligase (FadD), long-chain fatty acid transport protein (FadL), fatty acid kinase (FakA, FakB), acyl-ACP
963 thioesterase (FatA), iron transport protein (FatB), thioesterase 1/protease 1/lysophospholipase L1 (TesA),
964 phosphate acyltransferase (PlsX), CoenzymeA (CoA), acyl carrier protein (ACP). Thioesterases of interest
965 are bolded. **b.** Contigs from metagenomic sequencing data carrying the KOs of the bacterial acyl-CoA

966 thioesterases FatA and TesA were assigned to bacterial classes using Kraken2. Relative proportions (log10-
967 transformed coverage of contigs) of relevant bacterial classes are displayed. Remaining bacterial classes
968 were summarized as other. **c**. Levels of stearic acid measured in bacterial cultures (in relation to sterile
969 growth medium, shown as log*2*) of the Sonnenburg dataset published by Han *et al*. Families of the class
970 Clostridia are listed in red, while families of the class Bacteroidia are listed in blue. **d.** Relative abundance
971 (centered-log transformed total read counts) of stearate-producing and -consuming families of interest
972 (bolded in **c**) detected in murine fecal samples from KD-, SD-fed, KC and SC recipient mice at
973 endpoint. Boxplots show medians with 1st and 3rd quantiles. The whiskers from the hinges to the
974 smallest/largest values represent 1.5*inter-quartile range (IQR). Wilcoxon signed-rank test with
975 Bonferroni correction. Data shown in (**d**) are from n=9 SPF SD-fed and n=8 SPF KD-fed mice, pooled from
976 two independent experiments (**red and black**) and from n=8 mice per SC/KC condition (**gray and orange**).

977

978 **Figure 6. The microbial metabolite stearate exhibits anti-cancer effects. | a.** Schematic representation
979 of the dietary stearic acid supplementation experimental setup (created with BioRender.com). **b.**
980 Compositions of the control diet (CD) and the stearate-supplemented diet (SSD), with % of calories from
981 the indicated source. **c-d.** Stearic acid levels detected in serum (**c**) and fecal (**d**) samples from CD- and SSD-
982 fed mice, as detected by LC-MS. **e.** Colonic tumor burden in CD and SSD mice. **f.** Representative images of
983 colons from one CD and SSD mouse. Scale bar = 1mm. Data shows mean±SD from n=6 CD and n=5 SSD
984 mice in (**c**), from n=8 CD and n=8 SSD mice in (**d**). Two-sided Mann-Whitney test in (**c**) and (**d**). Data shows
985 mean±SD from n=8 CD and n=8 SSD mice in (**e**). Analysis of deviance of a negative-binomial generalized
986 linear model. **g-h.** HT29 proliferation over time (**g**) or scaled confluence at 72 hours (**h**) after treatment
987 with stearic acid or corresponding control (100µM, 150 µM, 200 µM, 250 µM, 300 µM). Data shows mean
988 (**g**) or mean±SD (**h**) from n=3 independent experiments, indicated by different datapoint shapes (**h**), each
989 with eight technical replicates per condition. **i.** ATP measurement (CellTiterGlo) of HT-29 cells at 72 hours

990 after treatment with stearic acid, oleic acid, dodecanoic acid or control (200 µM). Data shows mean±SD
991 of n=3 independent experiments (indicated by different datapoint shapes), each with eight technical
992 replicates. Two-way ANOVA with multiple comparisons in (**h**), (**i**). **j**. Principal component analysis of HT-29
993 cells treated with 200 µM of oleic, dodecanoic and stearic acid. **k.** Hallmark gene sets in stearic acid-
994 treated versus control cells. **l**. Cell cycle and apoptosis related gene expression in control, oleic,
995 dodecanoic and stearic acid-stimulated HT-29 cells and in tumor and matching normal tissue samples. **m-**
996 **n**. Caspase-3 activity in HT-29 (**m**) and HCT-116 (**n**) cells treated with stearic acid in presence or absence
997 of a broad caspase inhibitor (zVad). Staurosporine 2uM was used as a positive control. Data shown in (**j**),
998 (**k**), (**l**), (**m**) and (**n**) is from n=3 independent experiments. Data shows mean±SD of n=3 independent
999 experiments (indicated by different datapoint shapes), in (**m**) and (**n**). Ordinary one-way ANOVA in (m)
1000 and (n), data passed Shapiro-Wilk normality test.

1001

1002 **Figure 7. Functional ketogenic-diet-induced changes in the gut microbiome are responsible for its anti-**
1003 **cancer properties.**

1004 Ketogenic diet consumption leads to lasting functional changes in the gut microbiome, which are sufficient
1005 to reduce colonic tumor burden and which impact the luminal long-chain fatty acid pool. The enriched
1006 microbial product stearate demonstrates tumor-suppressing properties by inducing apoptosis in cancer
1007 cells and decreasing colonic Th17 immune cell populations.

1008

1009 **Extended data figure 1. | a.** Metadata of fecal sample donors. M=male, F=female. **b-d.** Relative
1010 abundance of the top 20 most abundant bacterial families (**b**), genera (**c**) and species (**d**) in human stool
1011 samples (CLR units)**. e.** Relative metabolite levels detected in human fecal samples, analyzed by
1012 untargeted LC-MS.

1013

1014 **Extended data figure 2. | a-b.** Mouse body weight (grams) over time (weeks) in the GF (**a**) and SPF (**b**)
1015 dietary experiments. Weight was not recorded between week five and ten (**a**) as no scale was available in
1016 the facility. **c.** Colon length (cm) in the GF dietary experiment at experimental endpoint. **d-e.** Heatmap of
1017 KD-induced changes in the immune cell compartment in relation to SD (log2foldchange) in the GF (**d**) and
1018 SPF (**e**) diet experiments as detected by flow cytometry. Stars overlaid on the heatmaps indicate *$p<0.05$,
1019 least squared means analysis. **f**. IL-17^+ $CD4^+$ T cells (counts) in the colons of SD and KD mice. **g-h**. Expression
1020 of S1008A in the colons of SD and KD mice in the GF (**g**) and SPF (**h**) dietary experiments, as detected by
1021 qPCR. **i**. Fecal lipocalin-2 levels (pg per gram of feces) in the SPF dietary experiment as detected by ELISA.
1022 Data is shown as mean±SD in (**a**), (**b**), (**c**), (**f**), (**g**), (**h**), and (**i**), Mann-Whitney U test. Data in (**a**), (**c**), (**d**), (**e**),
1023 (**f**) and (**g**) shows n=4 mice in the SD-fed condition and n=5 or 6 mice in the KD-fed condition from one
1024 experiment in the GF facility. Data in (**b**), (**h**) and (**i**) shows n=7 or 8 and 9 mice in the KD-fed condition and
1025 the SD-fed condition respectively, pooled from two independent experiments in the SPF facility.

1026

1027 **Extended data figure 3. | a.** Schematic representation of the dietary AOM experimental setup in the GF
1028 facility (created with BioRender.com). **b.** Mouse body weight (grams) over time (days) in mice
1029 administered 5HD. **c.** Colonic tumor burden at endpoint. **d.** Heatmap of immune cell population
1030 phenotyping of intra-epithelial lymphocytes (IEL), lamina propria (LP), mesenteric lymph nodes (MLN) and
1031 spleens of KD-fed mice in relation to SD-fed mice in GF mice (GF) or in mice gavaged with a mixture of
1032 stool samples from five healthy donors (5HD). Least-squared means analysis was performed on each
1033 combination of tissue and cell immune cell type using a linear model, however no statistically significant
1034 differences were found. **g.** One representative image of a section of liver stained with H&E per condition.
1035 Scale bar=500µm. Data in (**b**) and (**c**) shown as mean±SD. Mann-Whitney U test in (**c**)**.** Data in (**b**), (**c**) and

1036 (**d**) shows n=7 and 6 mice in the GF SD and KD conditions respectively and n=6 and 4 mice in the 5HD SD
1037 and KD conditions, respectively.

1038

1039 **Extended data figure 4. | a-b.** PCA (95% confidence interval) of plasma metabolites from mice in the GF
1040 (**a**) and SPF (**b**) diet experiments, as analyzed by united GC-MS and LC-MS analyses (**a**) and GC-MS analysis
1041 alone (**b**). **c-d.** Relative intensity of β-HB in plasma from mice in the GF (**c**) and SPF (**d**) diet experiments,
1042 as analyzed by GC-MS. **e-f.** Log_2foldchange of identified plasma bile acids in KD-fed mice in relation to SD-
1043 fed mice in the GF (**e**) and SPF (**f**) facilities, as analyzed UHPLC-MS. **g.** Schematic representation of the
1044 experimental setup of a Th17 cell differentiation assay (created with BioRender.com). **h-i.** Th17
1045 differentiation upon treatment with β-HB (10mM, 50mM, 100mM), acetone (1mM, 10mM, 100mM) or
1046 sodium acetoacetate (10mM, 100mM, 250mM) in (**h**), a lipid mixture (1%, 2%, 5%) in (**i**). Data in (**c**), (**d**),
1047 (**h**) and (**i**) is shown as mean±SD. Two-tailed Mann-Whitney U test in (**c**) and (**d**); Two-tailed unpaired T
1048 test with FDR correction in (**e**) and (**f**); Paired ordinary one-way ANOVA in (**h**) and (**i**). Paired ordinary one-
1049 way ANOVA comparing each set of ketone body dilutions to the control yielded no statistical significance
1050 in (**h**). Data in (**a**), (**c**) and (**e**) shows n=5 mice per condition. Data in (**b**), (**d**) and (**e**) shows n=9 mice in the
1051 SD-fed condition and n=7 mice in the KD-fed condition. Data in (**h**) shows n=5 biological replicates (mice)
1052 indicated by different datapoint shapes, from one experiment. Data in (**i**) shows n=6 biological replicates
1053 (mice) indicated by different datapoint shapes, pooled from two experiments. Abbreviations: not
1054 detected (n.d.), cholic acid (CA), hyocholic acid (HCA), chenodeoxycholic acid (CDCA), deoxycholic acid
1055 (DCA), 7-oxo-deoxycholic acid (7-oxo-DCA), murideoxycholic acid (MDCA), lithocholic acid (LCA),
1056 ursodeoxycholic acid (UDCA), hyodeoxycholic acid (HDCA), muricholic acids (α-MCA, β-MCA and ω-MCA),
1057 taurocholic acid (TCA), taurohyocholic acid (THCA), taurochenodeoxycholic acid (TCDCA),
1058 taurodeoxycholic acid (TDCA), taurolithocholic acid (TLCA), tauroursodeoxycholic acid (TUDCA),

1059 taurohyodeoxycholic acid (THDCA), tauro-α-muricholic acid (T-α-MCA), tauro-β-muricholic acid (T-β-MCA)
1060 and tauro-ω-muricholic acid (T-ω-MCA).

1061

1062 **Extended data figure 5. | a-b.** Colonic inner mucus layer thickness (in pixels, **a**) and representative images
1063 of Alcian Blue staining of colonic cryosections (**b**) in GF KD-fed and SD-fed mice. **c-d.** LPS (endotoxin units
1064 (EU) per milliliter) in plasma from GF (**c**) and SPF (**d**) KD-fed mice and SD-fed mice measured by ELISA. **e-f.**
1065 Colonic occludin gene expression (**e**) and protein expression (**f**) in KD and SD mice in the SPF dietary
1066 experiment, as measured by qPCR (**e**) and immunofluorescent staining (occludin-TRITC in red and DAPI
1067 nuclear stain in blue, one representative colon per condition is shown, scale bar = 200 µM, **f**). Two-tailed
1068 Mann-Whitney U test in (**a**), (**c**), (**d**), (**e**) and (**g**). Data in (**a**) shows n=4 SD and n=6 KD mice. Data in (**c**) and
1069 (**d**) shows n=4 mice per condition. Data in (**e**) shows n=6 mice per condition.

1070

1071 **Extended data figure 6. | a.** Mouse body weight (grams) over time (days) in the CMT experiment. **b-c.**
1072 Colonic occludin gene expression (**b**) and protein expression (**c**) in KC and SC mice, as measured by qPCR
1073 (**b**) and immunofluorescent staining (occludin-TRITC in red and DAPI nuclear stain in blue, one
1074 representative colon per condition is shown, scale bar = 200 µM, **c**). **d-e.** S100A8 (**e**) and IL-17 (**e**) gene
1075 expression in KC and SC mice in the CMT experiment, as measured by qPCR. Data is shown as mean±SD in
1076 (**a**), (**b**), (**d**) and (**e**). Two-tailed Mann-Whitney U test in (**b**), (**d**) and (**e**). Data in (**a**) shows n=16 mice per
1077 condition. Data in (**b**), (**d**) and (**e**) shows n=8 mice per condition.

1078

1079 **Extended data figure 7. | a.** Stearic acid levels detected in fecal samples from SPF KD- and SD-fed mice
1080 (Fig. 4**c**) by LC-MS (non-polar phase). Data is shown as mean±SD from n=9 KD mice and n=8 SD mice. **b.**

1081 Relative taxonomic assignment of contigs encoding for the selected KOs of interest at class level in fecal
1082 samples from KD- and SD-fed mice, and KC and SC recipient mice, at endpoint. Data shows n=8 SPF KD-
1083 fed mice and n=9 mice SPF SD-fed mice, pooled from two independent experiments, and n=8 KC and n=8
1084 SC recipient mice from one experiment. Shading of genes in red indicates synthesis-related genes, shading
1085 in gray indicates acyl-CoA thioesterases and shading in blue indicates genes involved in acquisition of
1086 extracellular long chain fatty acids. **c.** Levels of oleic acid (**left**) and palmitic acid (**right**) measured in
1087 bacterial cultures (in relation to sterile growth medium, shown as log*2*) of the Sonnenburg dataset
1088 published by Han *et al*. Families of the class Clostridia are listed in red, while families of the class
1089 Bacteroidia are listed in blue. **d.** Free long-chain fatty acid profiles (**left,** heatmap shows means) and free
1090 stearic acid content detected in SD and KD (**right,** shown as mean±SD). Two technical replicates per diet
1091 are shown.

1092

1093 **Extended data figure 8. | a.** Mouse body weight (grams) over time (days) in stearate-supplemented diet-
1094 fed (SSD) mice and control-diet-fed (CD) mice. **b.** Free long-chain fatty acid profiles (**left,** heatmap shows
1095 means) and free stearic acid content detected in SD and KD (**right,** shown as mean±SD). Two technical
1096 replicates per diet are shown. **c.** Fecal lipocalin-2 levels (pg per gram of feces) in CD and SSD mice as
1097 detected by ELISA. **d.** Frequency of IL-17+ CD4+ in colonic lamina propria in CD and SSD mice, as detected
1098 by flow cytometry. **e-f.** Th17 differentiation upon treatment with BSA-complexed dodecanoic acid, oleic
1099 acid and stearic acid (50µM, **e**) and with BSA-complexed palmitic and oleic acid (10µM, **f**). Data is shown
1100 as mean±SD in (**a**), (**b, right**), (**c**), (**d**), (**e**) and (**f**). Data in (**a**), (**c**) and (**c**) shows n=8 mice per condition. Data
1101 in (**e**) shows n=4 and data in (**f**) shows n=6 biological replicates (mice) indicated by different datapoint
1102 shapes, from one experiment each. Unpaired Mann-Whitney U test in (**c**). Unpaired T test in (**d**), data
1103 passed Shapiro-Wilk normality test p= 0.29. Paired ordinary one-way ANOVA in (**e**) and (**e**). **g-j.** HCT116
1104 (**g**) and Caco2 (**i**) proliferation over time and scaled HCT116 (**h**) and Caco2 (**j**) confluence at 72 hours after

1105 treatment with stearic acid or corresponding control (100µM, 150 µM, 200 µM, 250 µM, 300 µM). Data
1106 shows mean (**g**) and (**i**) or mean±SD (**h**) and (**j**) from n=3 independent experiments, indicated by different
1107 datapoint shapes, each with eight technical replicates per condition. Two-way ANOVA with multiple
1108 comparisons in (**h**) and (**h**). **k.** Heatmap showing the expression of apoptosis hallmark genesets in HT-29
1109 cells treated with dodecanoic acid, oleic acid and stearic acid (200µM). Labeled genes are identified as
1110 being differentially expressed in the DGE analysis ($|\log_2 FC| > 0.25$ and p-adj < 0.05). Data shown in (**k**) is
1111 from n=3 independent experiments.

1112

1113 **Extended data figure 9. | a.** Representative gating strategy of dendritic cells. **b.** Representative gating
1114 strategy of macrophages. **c.** Representative gating strategy of regulatory T cells. **d.** Representative gating
1115 strategy of $CD8^+$ T cells. **e.** Representative gating strategy of T helper 1 (subpanel 1) and T helper 2 cells
1116 (subpanel 2).

1117

1118 **Extended data figure 10. | a.** Representative gating strategy of innate lymphoid cells (ILC) - ILC1 (subpanel
1119 1), ILC2 (subpanel 2), ILC3 (subpanel 3). Transcription factors and cytokines are stained in two separate
1120 batches. **b.** Representative gating strategy of natural killer (subpanel 1) and natural killer T (subpanel 2)
1121 cells. **c.** Representative gating strategy of T helper 17 cells – transcription-factor-based phenotyping
1122 (subpanel 1), cytokine-based phenotyping (subpanel 2) and the combined strategy (subpanel 3).

1123

1124 **Acknowledgments**

1125 We acknowledge the contributions of the following people in the context of this project and thank
1126 them for their work: Dominik Ternes, Rubens Begaj, Martin Nurmik, Mohaned Benzarti and Monica
1127 Gabola (MDM group, DLSM) for assistance during organ processing at experimental endpoint; Ysaline

Bossicard (MDM group, DLSM) for tissue cryosectioning. We thank the LCSB Metabolomics and Lipidomics Platform (RRID:SCR_024769) for their technical and analytical support with our metabolomics samples, especially Xiangyi Dong, Floriane Gavotto and Christian Jäger. We further thank Aurélien Ginolhac (DLSM) for contributions to data pre-processing; Pau Perez Escriva (DLSM) for bacterial culturing; Djalil Coowar, Jennifer Behm, Julie Virolle, Cloe Ordrenneau and all other members of the Animal Facility Team (LCSB); Sara Gomez and Eliane Klein (DLSM) for maintenance of organoid and cell cultures; Rashi Halder for fecal sample 16s and WGS sequencing. The sequencing experiments presented in this paper were carried out at the LCSB sequencing platform (RRID: SCR_021931) at the University of Luxembourg. We also thank the donors who contributed their samples to the MuSt cohort, as well as Christelle Bahlawane (CIEC), Eve Herkenne (CIEC), Laetitia Garcia (CIEC), Ingrid Vreja (CIEC), and nurses from CIEC for contributing to this cohort. We thank Dr. Barbara Kofler for her feedback and discussions during the course of the project. The experiments presented in this paper were carried out using the high-performance computing facilities at the University of Luxembourg (https://hpc.uni.lu)[78]. BioRender (BioRender.com) was used for graphical illustration.

Funding

This work was supported by the Luxembourg National Research Fund (FNR) (grant nos. CORE/C16/BM/11282028 (E.L.), PoC/18/12554295 (E.L.), AFR AFR 17103240 (C.G.), PRIDE17/11823097 (M.T., M.K., L.d.N.) and CORE/15/BM/10404093 (P.W.)), by the Luxembourg National Research Fund and the Fondation Cancer Luxembourg (grant no. CORE/C20/BM/14591557 (E.L.)), AFR 17103240 as well as by the Fondation du Pélican de Mie and Pierre Hippert-Faber under the aegis of the Fondation de Luxembourg ('Pelican Grant'; M.T. and M.M.), a FNRS-Télévie grant to M.M., no. 7.4565.21-40007364), an Internal Research Project at the University of Luxembourg (MiDiCa—integrated analysis of the effects

1151 of microbiome-diet interactions on human colorectal adenocarcinoma enterocytes; E.L., P.W. and S.H.),
1152 the Fondation Cancer and the Fondation Kriibskrank Kanner Luxembourg (V.I.P), the Action LIONS Vaincre
1153 le Cancer Luxembourg and a European Research Council grant under the European Union's Horizon 2020
1154 research and innovation programme (grant agreement no. 863664 to P.W.). This project was also
1155 supported by the Doctoral School in Science and Engineering (M.T., M.K., M.M. and L.d.N.) and the
1156 Department of Life Sciences and Medicine at the University of Luxembourg. The funders had no role in
1157 study design, data collection and analysis, decision to publish or preparation of the manuscript.

1158

Figure 1

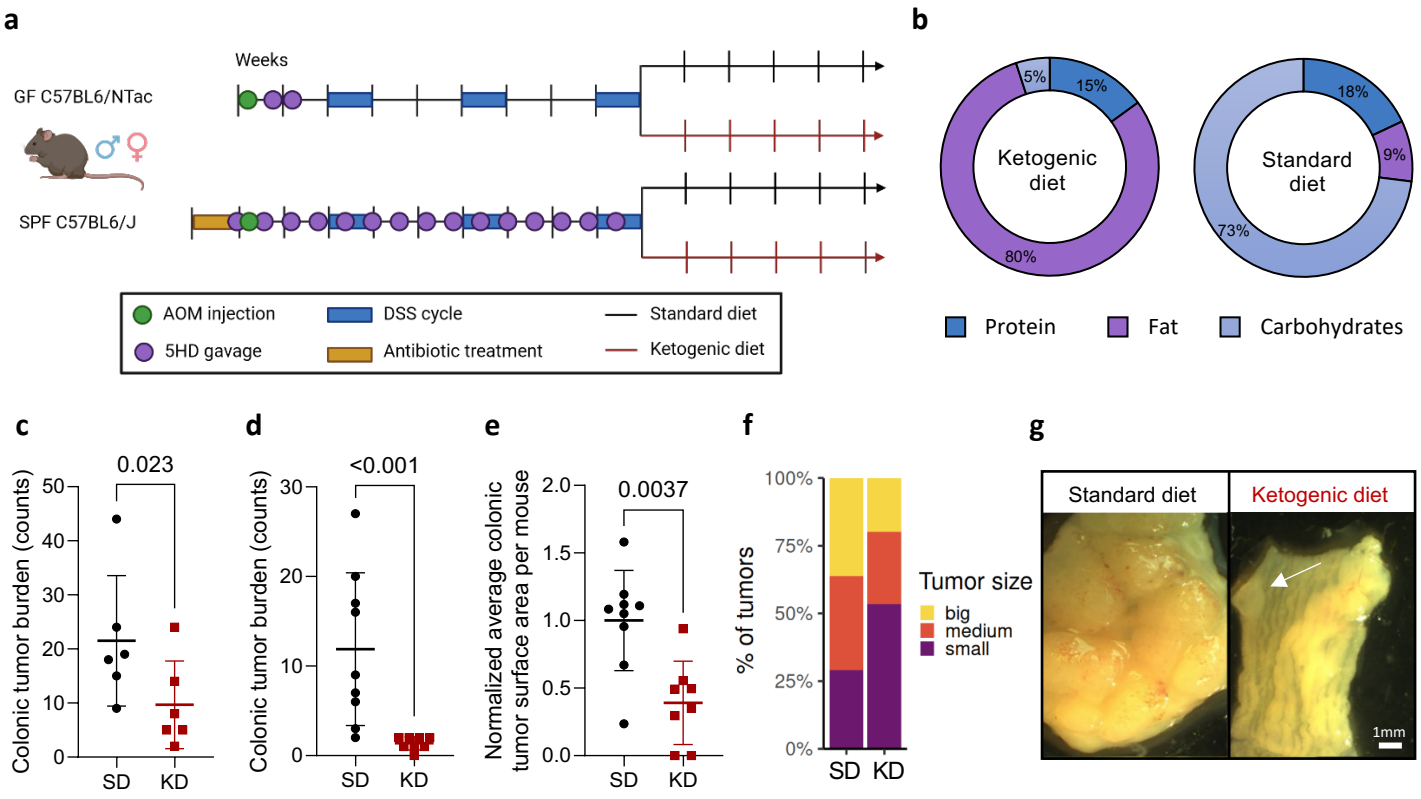
a
Weeks
GF C57BL6/NTac
SPF C57BL6/J
AOM injection
5HD gavage
DSS cycle
Antibiotic treatment
Standard diet
Ketogenic diet
b
Ketogenic diet
5%
15%
80%
Standard diet
18%
9%
73%
Protein
Fat
Carbohydrates
c
0.023
Colonic tumor burden (counts)
SD
KD
d
<0.001
Colonic tumor burden (counts)
SD
KD
e
0.0037
Normalized average colonic tumor surface area per mouse
SD
KD
f
% of tumors
SD
KD
Tumor size
big
medium
small
g
Standard diet
Ketogenic diet
1mm

Figure 2

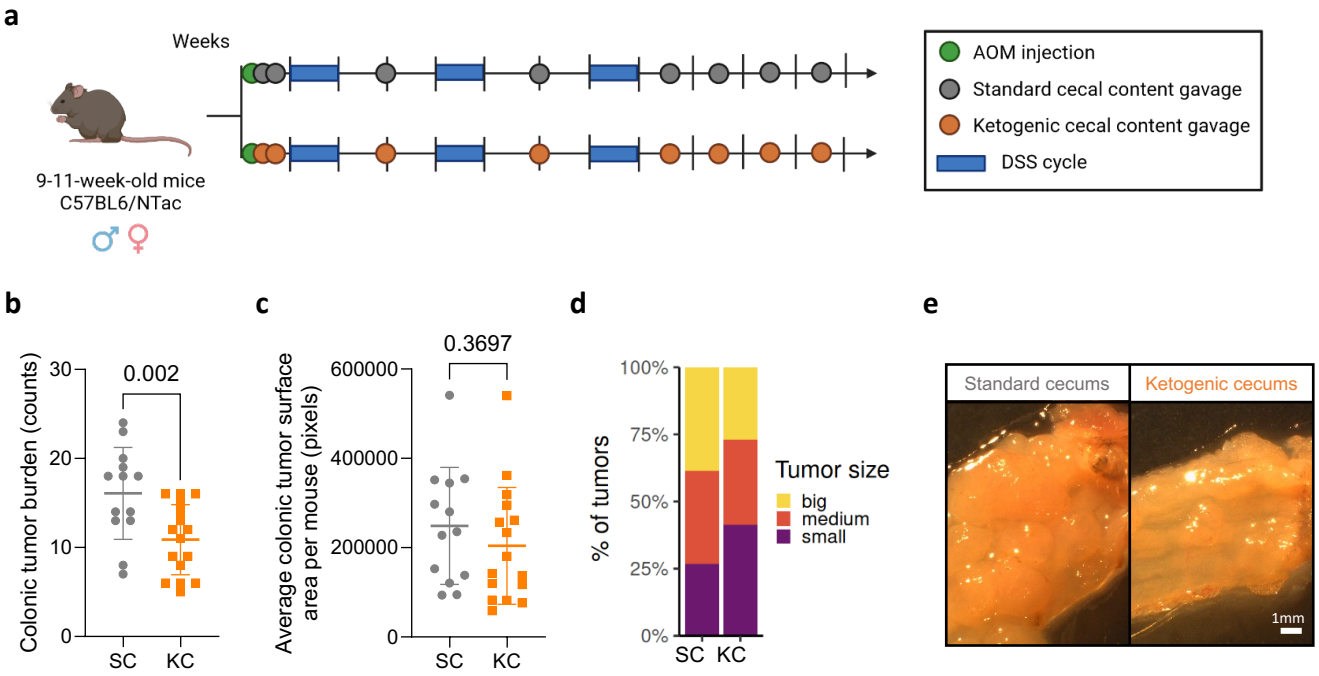
a
Weeks
9-11-week-old mice
C57BL6/NTac
AOM injection
Standard cecal content gavage
Ketogenic cecal content gavage
DSS cycle
b
Colonic tumor burden (counts)
0.002
SC
KC
c
Average colonic tumor surface area per mouse (pixels)
0.3697
SC
KC
d
% of tumors
Tumor size
big
medium
small
SC
KC
e
Standard cecums
Ketogenic cecums
1mm

Figure 3

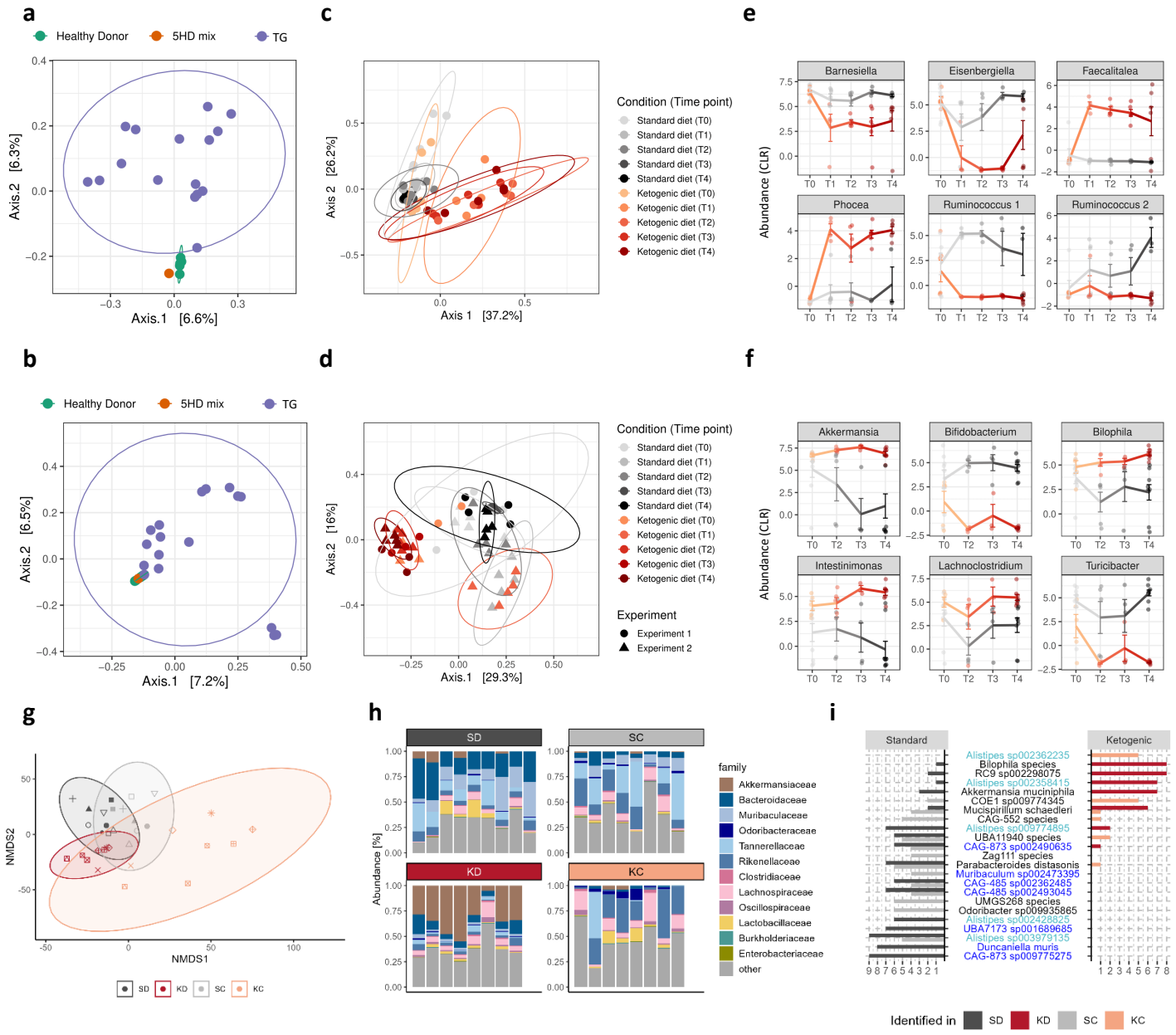
a
Healthy Donor
5HD mix
TG
Axis.2 [6.3%]
Axis.1 [6.6%]
b
Healthy Donor
5HD mix
TG
Axis.2 [6.5%]
Axis.1 [7.2%]
c
Axis 2 [26.2%]
Axis 1 [37.2%]
Condition (Time point)
Standard diet (T0)
Standard diet (T1)
Standard diet (T2)
Standard diet (T3)
Standard diet (T4)
Ketogenic diet (T0)
Ketogenic diet (T1)
Ketogenic diet (T2)
Ketogenic diet (T3)
Ketogenic diet (T4)
d
Axis.2 [16%]
Axis.1 [29.3%]
Condition (Time point)
Standard diet (T0)
Standard diet (T1)
Standard diet (T2)
Standard diet (T3)
Standard diet (T4)
Ketogenic diet (T0)
Ketogenic diet (T1)
Ketogenic diet (T2)
Ketogenic diet (T3)
Ketogenic diet (T4)
Experiment
Experiment 1
Experiment 2
e
Barnesiella
Eisenbergiella
Faecalitalea
Phocea
Ruminococcus 1
Ruminococcus 2
Abundance (CLR)
T0 T1 T2 T3 T4
f
Akkermansia
Bifidobacterium
Bilophila
Intestinimonas
Lachnoclostridium
Turicibacter
Abundance (CLR)
T0 T2 T3 T4
g
NMDS2
NMDS1
SD
KD
SC
KC
h
SD
SC
KD
KC
Abundance [%]
family
Akkermansiaceae
Bacteroidaceae
Muribaculaceae
Odoribacteraceae
Tannerellaceae
Rikenellaceae
Clostridiaceae
Lachnospiraceae
Oscillospiraceae
Lactobacillaceae
Burkholderiaceae
Enterobacteriaceae
other
i
Standard
Ketogenic
Alistipes sp002362235
Bilophila species
RC9 sp002298075
Alistipes sp002358415
Akkermansia muciniphila
COE1 sp009774345
Mucispirillum schaedleri
CAG-552 species
Alistipes sp009774895
UBA11940 species
CAG-873 sp002490635
Zag111 species
Parabacteroides distasonis
Muribaculum sp002473395
CAG-485 sp002362485
CAG-485 sp002493045
UMGS268 species
Odoribacter sp009935865
Alistipes sp002426625
UBA7173 sp001689685
Alistipes sp003979135
Duncaniella muris
CAG-873 sp009775275
Identified in
SD
KD
SC
KC

Figure 4

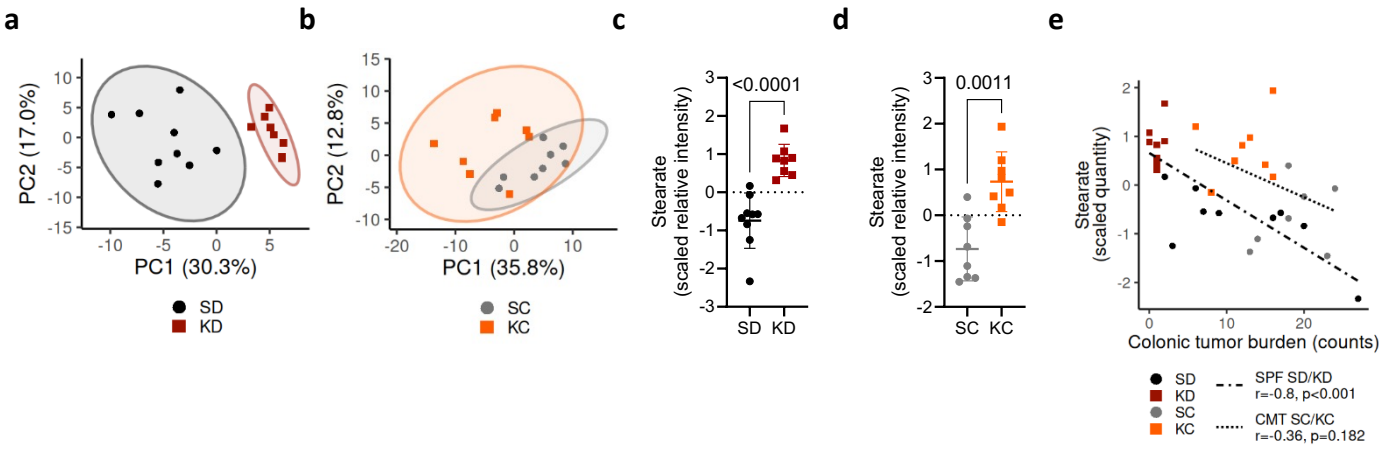
a
PC2 (17.0%)
PC1 (30.3%)
SD
KD
b
PC2 (12.8%)
PC1 (35.8%)
SC
KC
c
<0.0001
Stearate
(scaled relative intensity)
SD KD
d
0.0011
Stearate
(scaled relative intensity)
SC KC
e
Stearate
(scaled quantity)
Colonic tumor burden (counts)
SD
KD
SC
KC
SPF SD/KD
r=-0.8, p<0.001
CMT SC/KC
r=-0.36, p=0.182

Figure 5

a

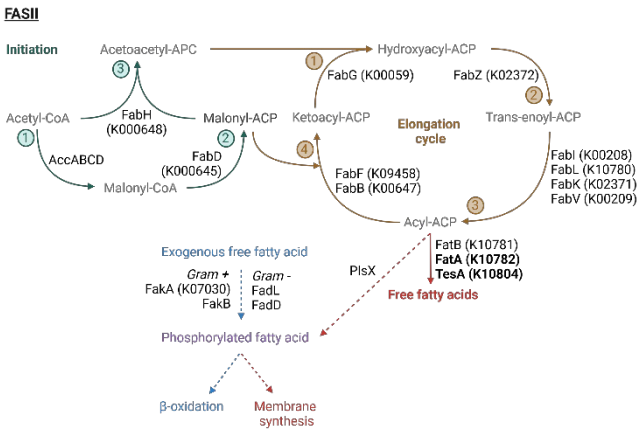

b

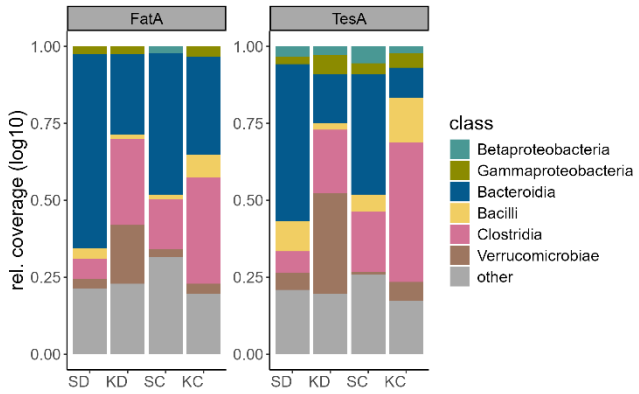

c

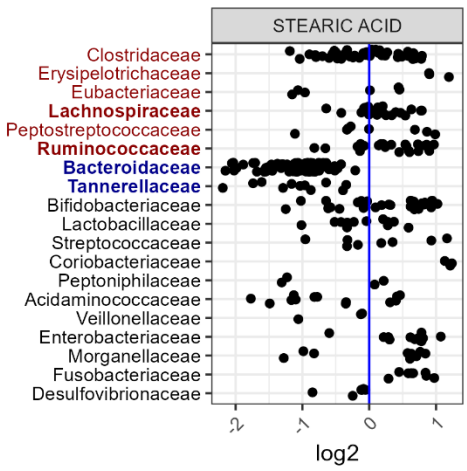

d

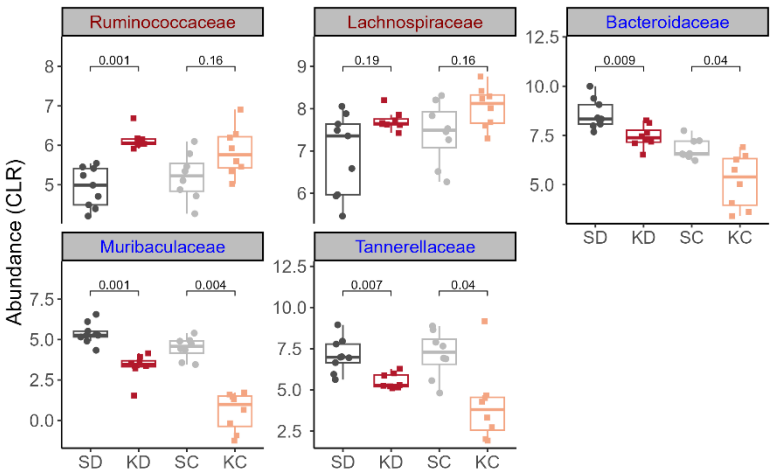

Figure 6

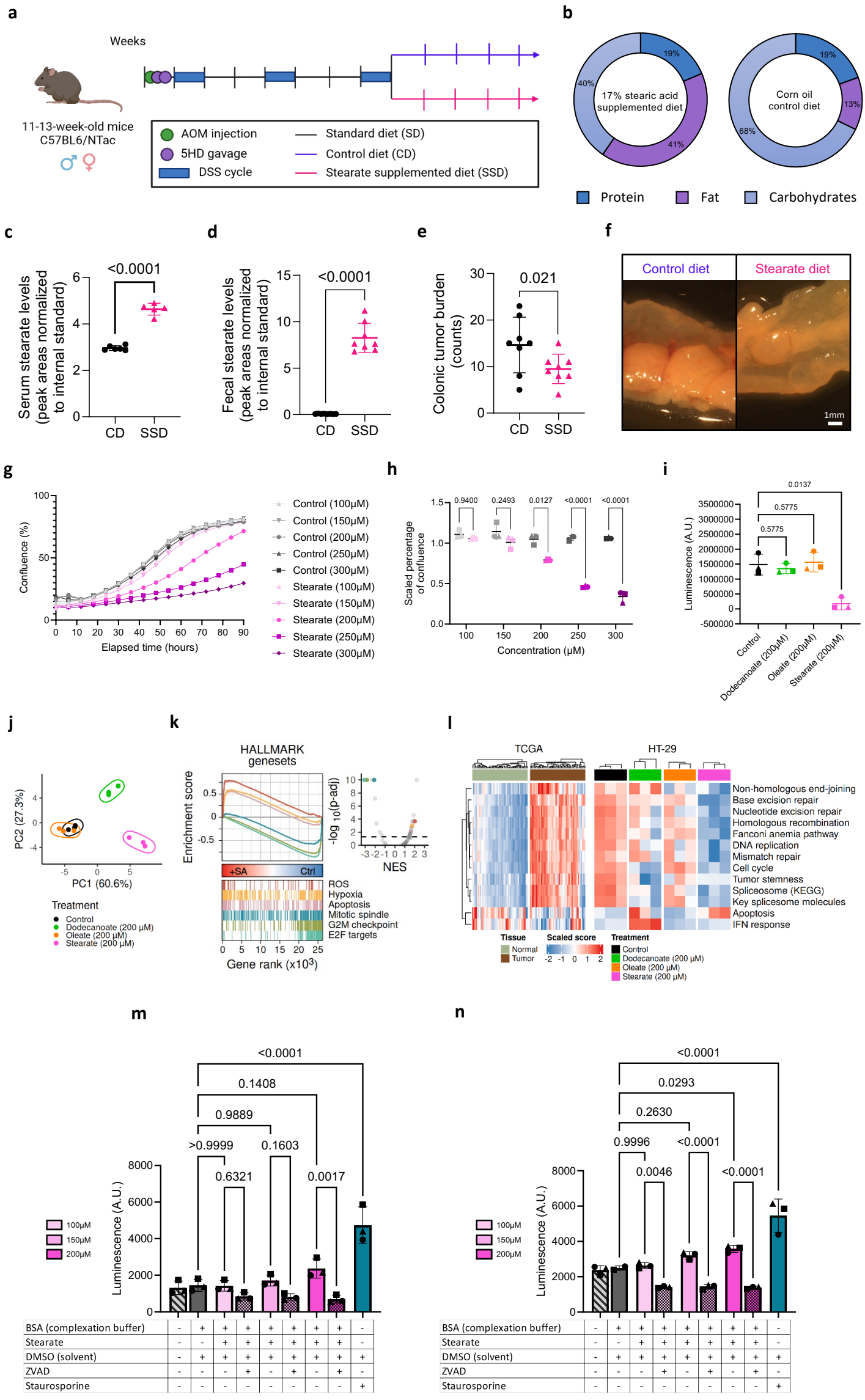
a
Weeks
11-13-week-old mice
C57BL6/NTac
AOM injection
5HD gavage
DSS cycle
Standard diet (SD)
Control diet (CD)
Stearate supplemented diet (SSD)
b
17% stearic acid supplemented diet
Corn oil control diet
19%
41%
40%
13%
68%
Protein
Fat
Carbohydrates
c
Serum stearate levels (peak areas normalized to internal standard)
<0.0001
CD
SSD
d
Fecal stearate levels (peak areas normalized to internal standard)
<0.0001
e
Colonic tumor burden (counts)
0.021
f
Control diet
Stearate diet
1mm
g
Confluence (%)
Elapsed time (hours)
Control (100μM)
Control (150μM)
Control (200μM)
Control (250μM)
Control (300μM)
Stearate (100μM)
Stearate (150μM)
Stearate (200μM)
Stearate (250μM)
Stearate (300μM)
h
Scaled percentage of confluence
0.9400
0.2493
0.0127
<0.0001
<0.0001
Concentration (μM)
i
Luminescence (A.U.)
0.0137
0.5775
0.5775
Control
Dodecanoate (200μM)
Oleate (200μM)
Stearate (200μM)
j
PC2 (27.3%)
PC1 (60.6%)
Treatment
Control
Dodecanoate (200 μM)
Oleate (200 μM)
Stearate (200 μM)
k
HALLMARK genesets
Enrichment score
+SA
Ctrl
ROS
Hypoxia
Apoptosis
Mitotic spindle
G2M checkpoint
E2F targets
Gene rank (x10³)
-log 10(p-adj)
NES
l
TCGA
HT-29
Non-homologous end-joining
Base excision repair
Nucleotide excision repair
Homologous recombination
Fanconi anemia pathway
DNA replication
Mismatch repair
Cell cycle
Tumor stemness
Spliceosome (KEGG)
Key splicesome molecules
Apoptosis
IFN response
Tissue
Normal
Tumor
Scaled score
Treatment
Control
Dodecanoate (200 μM)
Oleate (200 μM)
Stearate (200 μM)
m
<0.0001
0.1408
0.9889
>0.9999
0.1603
0.6321
0.0017
Luminescence (A.U.)
100μM
150μM
200μM
BSA (complexation buffer)
Stearate
DMSO (solvent)
ZVAD
Staurosporine
n
<0.0001
0.0293
0.2630
0.9996
<0.0001
0.0046
<0.0001
Luminescence (A.U.)
100μM
150μM
200μM
BSA (complexation buffer)
Stearate
DMSO (solvent)
ZVAD
Staurosporine

Figure 7

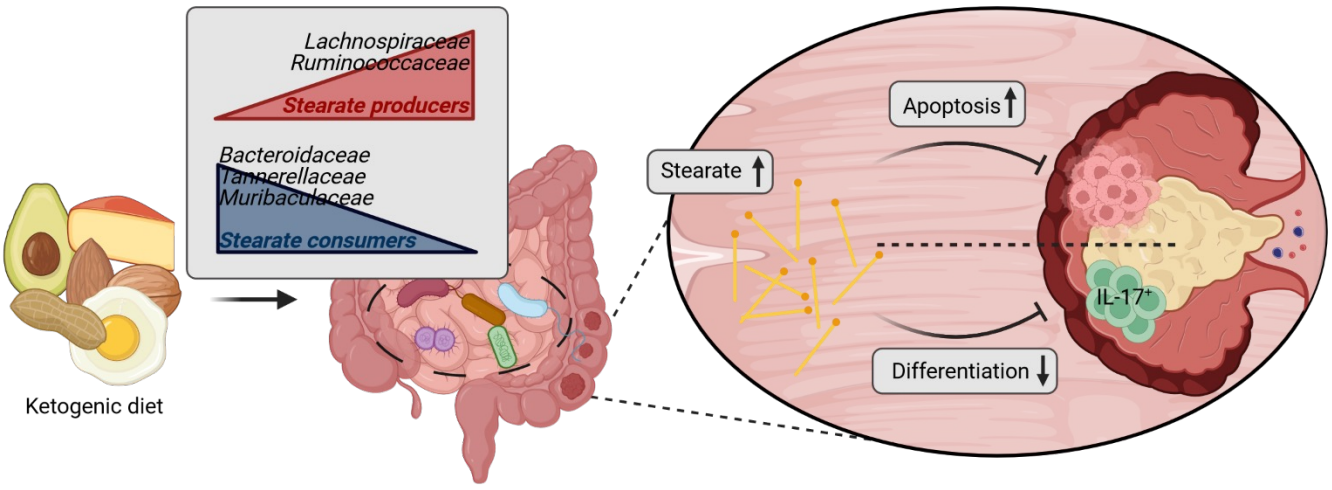
Lachnospiraceae
Ruminococcaceae
Stearate producers
Bacteroidaceae
Tannerellaceae
Muribaculaceae
Stearate consumers
Ketogenic diet
Stearate
Apoptosis
Differentiation
IL-17+